

# **Gross Moist Stability Analysis:**

## **Assessment of Satellite-based Products in the GMS Plane**

Kuniaki Inoue\*

*NOAA/GFDL, Princeton, New Jersey*

Larissa E. Back

*University of Wisconsin-Madison, Madison, Wisconsin*

\* *Corresponding author address:* Kuniaki Inoue, Geophysical Fluid Dynamics Laboratory/NOAA,  
Princeton University Forrestal Campus, 201 Forrestal Rd., Princeton, NJ 08540.  
E-mail: kuniaki.inoue@noaa.gov

## ABSTRACT

10 New diagnostic applications of the gross moist stability (GMS) are proposed  
11 with demonstrations using satellite-based data. The plane of the divergence  
12 of column moist static energy (MSE) against the divergence of column dry  
13 static energy (DSE), referred to as the GMS plane here, is utilized. In this  
14 plane, one can determine whether the convection is in the amplifying phase  
15 or in the decaying phase; if a data point lies below/above a critical line in the  
16 GMS plane, the convection is in the amplifying/decaying phase. The GMS  
17 plane behaves as a phase plane in which each convective life-cycle can be  
18 viewed as an orbiting fluctuation around the critical line, and this property  
19 is robust even on the MJO time-scale. This phase plane behavior indicates  
20 that values of the GMS can qualitatively predict the subsequent convective  
21 evolution. This study demonstrates that GMS analyses possess two different  
22 aspects: time-dependent and quasi-time-independent aspects. Transitions of  
23 time-dependent GMS can be visualized in the GMS plane as an orbiting fluctuation  
24 around the quasi-time-independent GMS line. The time-dependent  
25 GMS must be interpreted differently from the quasi-time-independent one,  
26 and the latter is the GMS relevant to moisture-mode theories. The authors  
27 listed different calculations of the quasi-time-independent GMS: (i) as a regression  
28 slope from a scatter plot, and (ii) as a climatological quantity which  
29 is the ratio of climatological MSE divergence to climatological DSE divergence.  
30 It is revealed that the latter, climatological GMS, is less appropriate as  
31 a diagnostic tool. Geographic variations in the quasi-time-independent GMS  
32 are plotted.

## 33 1. Introduction

34 It is well known that tropical convection and column-integrated water vapor (aka. precipitable  
35 water) are tightly related. Past work showed that there is a positive correlation between precip-  
36 itable water and precipitation (e.g., Raymond 2000; Bretherton et al. 2004; Neelin et al. 2009; Ma-  
37 sunaga 2012). This moisture-precipitation relationship plays a key role in an interaction between  
38 convection and associated large-scale circulations in the tropics; the ensemble of subgrid-scale  
39 convection alters large-scale circulations, and the large-scale circulations, in turn, change the lo-  
40 cal environment to be favorable or unfavorable for the convection via changing the local moisture  
41 condition. In this study, we present new diagnostic applications of a conceptual quantity called the  
42 gross moist stability (GMS) to investigate that interaction.

43 Column-integrated moist static energy (MSE) budgets are useful for investigating tropical con-  
44 vective disturbances. Temperature anomalies are small in the deep tropics owing to a large Rossby  
45 radius (e.g., Charney 1963; Bretherton and Smolarkiewicz 1989), which leads to a framework  
46 called the weak temperature gradient approximation (WTG; Sobel and Bretherton 2000; Sobel  
47 et al. 2001). This property of the tropics indicates that analyses of column MSE budgets approxi-  
48 mately tell us about the processes associated with the growth and decay of precipitable water. And  
49 these analyses are most likely if not always accompanied by a quantity called the GMS.

50 The GMS, which represents the efficiency of the advective export of MSE by large-scale circu-  
51 lations associated with convection, was originally coined by Neelin and Held (1987) with a simple  
52 two-layer atmospheric model. Two decades later, Fuchs and Raymond (2007) and Raymond et al.  
53 (2007) expanded this idea by defining a relevant quantity called the normalized GMS (NGMS)  
54 to include more general atmospheric structures. Since then, different authors have used slightly  
55 different definitions of the NGMS [see a review by Raymond et al. (2009)], but the philosophies

56 behind them are the same; they all represent the amount of MSE (or moist entropy) exported per  
57 unit intensity of convection. In this study, the NGMS is simply called the GMS.

58 The GMS represents a feedback effect; when ignoring diabatic effects, negative GMS corre-  
59 sponds to a positive feedback in which moist regions become moister and dry regions become  
60 drier due to atmospheric motions (e.g., Sessions et al. 2010). Negative values of the GMS are  
61 associated with the intensification of convection via a positive feedback loop associated with at-  
62 mospheric motions. Recent diagnostic studies showed that time-dependent GMS is a useful diag-  
63 nostic tool to study the intensification of convection; for instance, they found that a reduction of the  
64 GMS is a precursor of the onset of deep strong convection in meso-scale convective disturbances  
65 (e.g., Masunaga and L’Ecuyer 2014; Inoue and Back 2015b). In this work, we further examine  
66 the relationship between GMS and convective growth and decay. We show that convective life-  
67 cycles (both several-day, as well as the MJO) can be represented in a phase plane of column MSE  
68 divergence versus column dry static energy (DSE) divergence.

69 Recently, the GMS has gained increasing attention because the idea is growing that the Madden-  
70 Julian oscillation (MJO) is a moisture mode (e.g., Neelin and Yu 1994; Sobel et al. 2001; Sobel  
71 and Gildor 2003; Fuchs and Raymond 2002, 2005, 2007; Raymond and Fuchs 2007; Sugiyama  
72 2009; Sobel and Maloney 2012, 2013; Adames and Kim 2016). According to this theory, a version  
73 of the GMS (often including some diabatic effects and hence called the effective GMS) plays a  
74 crucial role in the destabilization of the mode corresponding to the MJO.

75 However, the association between the GMS and moisture-mode stability in the real atmosphere  
76 is complex. Most of the moisture-mode theories are based on linear stability analysis. The method  
77 of the linear stability analysis consists of introducing sinusoidal disturbances on the “background”  
78 state to be examined and determining whether the background state demands the growth or decay  
79 of the introduced disturbances. Thus, what determines the stability of modes are its background

80 state, and the GMS associated with the moisture-mode stability has to be “background GMS”.  
81 However, background GMS can be estimated in a variety of different ways. The pioneering work  
82 by Yu et al. (1998) showed global maps of a version of background GMS. These authors, however,  
83 made strong assumptions about the structure of the vertical motion profile, which are likely not  
84 borne out in the real world (e.g., Back and Bretherton 2006). In this study, we clarify how to  
85 assess time-dependent and background components of the GMS separately using satellite data.  
86 The methodology can also be compared to other data sets like reanalysis and numerical model  
87 output.

88 The rest of this paper is structured as follows. This study is verification and extensions of the  
89 ideas proposed by Inoue and Back (2015b), which are briefly summarized in the next section.  
90 Section 3 presents the descriptions of the data sets and the choice of the spatial domains for the  
91 analyses. Using those data sets, we verify the proposed ideas in sections 4a and 4b. We also  
92 propose in section 4c a novel diagnostic framework in which convective life-cycles are plotted in  
93 a phase plane of column MSE divergence versus column DSE divergence, which we refer to as  
94 the GMS plane analysis. This illustrates transient properties of the GMS throughout a convec-  
95 tive life-cycle. Furthermore, in section 4d, we examine the properties of quasi-time-independent  
96 “background GMS”, and show geographic variability of this quantity. In section 4e, we briefly  
97 demonstrate the GMS plane analysis on the MJO time-scale using field campaign data. A dis-  
98 cussion about the GMS plane analysis and what circumstances it is relevant to are presented in  
99 section 5a. In section 5b, we discuss how to calculate the GMS relevant to moisture-mode in-  
100 stability, and why the time-dependent version of the GMS does not represent the stability of a  
101 moisture mode. Section 6 concludes this study.

## 2. Summary of Inoue and Back (2015b)

Following Yanai et al. (1973), we start with the vertically integrated energy and moisture budget equations:

$$\frac{\partial \langle s \rangle}{\partial t} = -\nabla \cdot \langle s \mathbf{v} \rangle + \langle Q_R \rangle + LP + H, \quad (1)$$

$$\frac{\partial \langle Lq \rangle}{\partial t} = -\nabla \cdot \langle Lq \mathbf{v} \rangle + LE - LP, \quad (2)$$

where  $s \equiv c_p T + gz$  is dry static energy (DSE);  $c_p T$  is enthalpy;  $gz$  is geopotential;  $Q_R$  is radiative heating rate;  $L$  is the latent heat of vaporization;  $P$  is precipitation;  $H$  is surface sensible heat flux;  $q$  is water vapor mixing ratio;  $E$  is surface evaporation; the angle brackets represent a mass-weighted column-integration from surface pressure to 100 hPa; and the other terms are in accordance with the meteorological conventions. We neglected the residual in these equations.

When considering a time-scale longer than a diurnal cycle, the Eulerian tendency of column DSE is much smaller than that of precipitable water in the deep tropics. Thus, on such a time-scale, adding Eqs. 1 and 2 approximately yields

$$\frac{\partial \langle Lq \rangle}{\partial t} \simeq -\nabla \cdot \langle h \mathbf{v} \rangle + \langle Q_R \rangle + S, \quad (3)$$

where  $h \equiv s + Lq$  is moist static energy (MSE) and  $S \equiv LE + H$  is surface fluxes (generally  $H$  is negligible over the tropical oceans).

As claimed by past studies, there is a positive correlation<sup>1</sup> between precipitation and precipitable water. Thus we have the following proportionality:

$$\frac{\partial P}{\partial t} \sim \frac{\partial \langle q \rangle}{\partial t}. \quad (4)$$

This relationship indicates that when the RHS of Eq. 3 is positive/negative, the convection amplifies/decays. Although this seems to be an oversimplification, we will show it describes convective amplification and decay very well.

---

<sup>1</sup>The actual relationship is in a nonlinear form (exponential or power law). This study is not sensitive to those details.

121 It must be cautioned here that the words “amplification” and “decay” of local convection in this  
 122 study are used to mean differently from the words “destabilization” and “stabilization” of linear  
 123 modes, and thus those must not be confused with each other. The destabilization of linear modes  
 124 means increase in the amplitude of sinusoidal waves; positive anomalies become more positive  
 125 and negative anomalies become more negative. In contrast, the amplification of local convection  
 126 simply means intensification of convection in the Eulerian frame; we cannot say the whole mode  
 127 is destabilized simply because convection at one location amplifies.

128 Inoue and Back (2015b) did not examine Eq. 3 as it is, but they divided it by  $\nabla \cdot \langle s\mathbf{v} \rangle$ , which  
 129 represents the intensity of convection (or convective heating), converting the MSE budget equation  
 130 into a unitless efficiency equation:

$$\nabla \cdot \langle s\mathbf{v} \rangle^{-1} \frac{\partial \langle Lq \rangle}{\partial t} \simeq -(\Gamma - \Gamma_C), \quad (5)$$

131 where

$$\Gamma \equiv \frac{\nabla \cdot \langle h\mathbf{v} \rangle}{\nabla \cdot \langle s\mathbf{v} \rangle}, \quad (6)$$

$$\Gamma_C \equiv \frac{D}{\nabla \cdot \langle s\mathbf{v} \rangle}, \quad (7)$$

133  $D \equiv \langle Q_R \rangle + S$  is the diabatic source<sup>2</sup>.  $\Gamma$  is the (normalized) GMS, and  $\Gamma_C$  is an analogue of the  
 134 GMS named the critical GMS by Inoue and Back (2015b), which represents the contribution of the  
 135 diabatic source to column moistening.  $\Gamma - \Gamma_C$  is collectively called the drying efficiency because it  
 136 represents the efficiency of the loss of water vapor due to convection. This drying efficiency may  
 137 appear to be a version of the effective GMS (e.g., Su and Neelin 2002; Bretherton and Sobel 2002;  
 138 Peters and Bretherton 2005; Sobel and Maloney 2012; Adames and Kim 2016), and is close to the  
 139 effective GMS used by Hannah and Maloney (2014) and Sakaeda and Roundy (2016). However,

---

<sup>2</sup>In Inoue and Back (2015b), this was called the diabatic “forcing”. But the word “forcing” might be misleading because radiative heating and surface fluxes are, to some extent, an intrinsic property of convection instead of external “forcing”. Thus we simply call it the diabatic (MSE) source in this study.



140 the drying efficiency computed in this study must be interpreted as a different quantity from the  
 141 effective GMS used in theoretical studies. Hence, we refer to it as the drying efficiency rather  
 142 than the effective GMS. We clarify the distinction between them, together with the distinction  
 143 between the GMS computed as a time-dependent quantity and the one used in theoretical studies,  
 144 in section 5b.

145 Equation 5 has two benefits that Eq. 3 doesn't possess. First, because Eq. 5 is independent of  
 146 a convective intensity, we can take composites of all convective events with different intensities.  
 147 According to Eqs. 4 and 5, we can define two convective phases:

$$\Gamma - \Gamma_C < 0, \quad (8a)$$

$$\Gamma - \Gamma_C > 0, \quad (8b)$$

148 namely, the amplifying phase and the decaying phase, respectively. These relationships hold only  
 149 when the denominator of the drying efficiency,  $\nabla \cdot \langle s\mathbf{v} \rangle$ , is positive. We generalize this condition  
 150 to include the whole convective life-cycle by utilizing the GMS plane in section 4c.

151 The second benefit, which we verify in section 4b, is that the critical GMS  $\Gamma_C$  turns out to be  
 152 relatively constant. That simplifies the phases of Eqs. 8a and 8b into

$$\Gamma - \gamma < 0, \quad (9a)$$

$$\Gamma - \gamma > 0, \quad (9b)$$

153 where  $\gamma$  is some constant that is explained in more detail in sections 4b and 4d. Those phases  
 154 indicate that when the GMS is smaller/bigger than some critical constant, the convection ampli-  
 155 fies/decays.

### 3. Data description

From satellite views, we can observe the RHSs of the following equations:

$$\nabla \cdot \langle s\mathbf{v} \rangle \simeq \langle Q_R \rangle + LP + H, \quad (10)$$

$$\nabla \cdot \langle h\mathbf{v} \rangle \simeq \langle Q_R \rangle + S - \frac{\partial \langle Lq \rangle}{\partial t}. \quad (11)$$

In these equations, the column DSE tendency, which is much smaller than the other terms (e.g., Inoue and Back 2015b), was neglected. By using satellite-based data, we can compute the GMS  $\Gamma$ , critical GMS  $\Gamma_C$  and drying efficiency  $\Gamma - \Gamma_C$  as follows:

$$\Gamma = \frac{\langle Q_R \rangle + S - \partial \langle Lq \rangle / \partial t}{\langle Q_R \rangle + LP + H}, \quad (12)$$

$$\Gamma_C = \frac{\langle Q_R \rangle + S}{\langle Q_R \rangle + LP + H}, \quad (13)$$

$$\Gamma - \Gamma_C = -\frac{\partial \langle Lq \rangle / \partial t}{\langle Q_R \rangle + LP + H}. \quad (14)$$

The values of  $\nabla \cdot \langle s\mathbf{v} \rangle$  and  $\nabla \cdot \langle h\mathbf{v} \rangle$  were computed as the residual of Eqs. 10 and 11. The procedures of the data treatments are summarized in Fig. 1, which consist of three steps: removal of diurnal cycles, spatial average, and removal of seasonality.

Diurnal cycles need to be removed from all the budget terms otherwise we cannot neglect the column DSE tendency (e.g., Inoue and Back 2015b). The methodologies of diurnal-cycle removal depend on the data sets, which are described more specifically in the next subsection. The spatial grid size was changed into  $2^\circ \times 2^\circ$  by taking a spatial average in order to minimize sampling errors. Furthermore, we removed seasonality (or variability with periodicity longer than a month) from all the terms in order to minimize the effects of a seasonal convergence-zone shift. More detailed descriptions are presented in the following.

174 *a. Data source and procedure*

175 *Precipitable water* The precipitable water retrievals used in this study are derived from the  
176 TRMM Microwave Imager (TMI), a series of Special Sensor Microwave Imager (SSM/I F13,  
177 F14, F15, and F16) on Defense Meteorological Satellite Program (DMSP) satellites, and Ad-  
178 vanced Micro-wave Scanning Radiometer-Earth Observing System (AMSR-E) on *Aqua*. The data  
179 sets are provided by Remote Sensing Systems (RSS; Wentz et al. 2012, 2014, 2015).

180 For removing the diurnal cycles, we took an ensemble average of all the precipitable water data  
181 from the different satellite sensors listed above. Since each sensor flies over a given place at  
182 different local time, and diurnal cycles of precipitable water are not so large (not shown here),  
183 we expect this method minimizes the contamination due to the diurnal cycles. This method also  
184 allows us to obtain daily precipitable water data over the entire tropical ocean so that we can  
185 compute a snapshot of precipitable water tendency with center differencing over two days at any  
186 time and place over the whole tropical ocean. The precipitable water tendency data ( $0.25^\circ \times 0.25^\circ$   
187 grids) were spatially averaged into  $2^\circ \times 2^\circ$  grids.

188 Next, we removed variability with periodicity longer than one month as follows. First, we took  
189 a monthly average of the anomalies of the data to construct a monthly anomalous time-series.  
190 Then by applying a spline interpolation to that monthly time-series, we constructed a smoothed  
191 seasonality time-series at each day, which was subtracted from the daily data. By this method, we  
192 expect the effects associated with the seasonal ITCZ shift are minimized. This methodology also  
193 removed most of the MJO variability from the data set. Analyses of MJO-time-scale variability  
194 were done separately using different data, which are briefly shown in section 4e.

195 *Radiative heating* The radiative heating estimates based on the TMI are derived with the algo-  
196 rithm called the Hydrologic cycle and Earth's Radiation Budget (HERB: L'Ecuyer and Stephens

2003, 2007). The raw data used here, which exist only over the TMI swath, are instantaneous,  
0.5°×0.5° averages. For a vertical integration, we used the geopotential from the Interim European  
Center for Medium-Range Weather Forecasts Re-analysis (ERA-Interim; Dee et al. 2011), which  
is the only non-satellite data we used in this study. The grid size of the geopotential (~0.7°×0.7°)  
was changed into the same one as the radiative heating with a linear interpolation.

The diurnal cycles of the column radiative heating were computed based on the property of a  
sun-asynchronous TRMM orbit. We constructed the climatological diurnal cycles at each place  
by sorting the data array into 6-hourly bins, and taking an average within those bins. Those  
constructed diurnal cycles were removed from the raw data at each place. The column radiative  
heating data with diurnal cycles removed were spatially averaged into 2°×2° grids. Finally, the  
seasonality computed with a spline interpolation was removed in the same way as for the precip-  
itable water.

*Precipitation* For precipitation, we used version 7 of daily TRMM Multi-satellite Precipitation  
Analysis (TMPA) known as the 3B42 product (Huffman et al. 2007, 2010). The daily raw data  
given in 0.25°×0.25° grids were spatially averaged into 2°×2° grids, and a smoothed seasonality  
was removed in the same way as described above.

*Surface fluxes* The surface flux data including surface sensible heat flux and surface evaporation  
were obtained from SeaFlux (Curry et al. 2004), which is a data set relying almost exclusively on  
satellite observations. The 6-hourly, 0.25°×0.25° raw data were regridded into daily, 2°×2° grids  
with a daily and spatial average. Similarly to the other variables, a spline-interpolated seasonality  
was removed.

## 218 *b. Spatial domain for analysis*

219 For the analyses, we chose four spatial domains, depicted in Fig. 2, from the basins of the  
220 Indian Ocean (IO), the western Pacific Ocean (WP), the central-eastern Pacific Ocean (EP), and  
221 the Atlantic Ocean (AO). The regions surrounded by the polygons in Fig. 2 are analyzed separately  
222 in the following sections.

223 First, we set the rectangular boxes defined by ( $5^{\circ}\text{S}$ – $5^{\circ}\text{N}$ ,  $60^{\circ}\text{E}$ – $90^{\circ}\text{E}$ ), ( $5^{\circ}\text{S}$ – $5^{\circ}\text{N}$ ,  $150^{\circ}\text{E}$ – $180^{\circ}\text{E}$ ),  
224 ( $0^{\circ}$ – $15^{\circ}\text{N}$ ,  $190^{\circ}\text{E}$ – $250^{\circ}\text{E}$ ), ( $0^{\circ}$ – $15^{\circ}\text{N}$ ,  $300^{\circ}\text{E}$ – $360^{\circ}\text{E}$ ) for IO, WP, EP, and AO, respectively. And  
225 the regions with the mean precipitation (from 2000 to 2007) greater than 5 mm/day were chosen  
226 for the analyses. Over these regions, the quantities of interest, which are discussed in section 4d,  
227 are fairly homogeneous.

228 There are 70, 74, 88, and 47 grids surrounded by the boundaries for IO, WP, EP, and AO,  
229 respectively. In each domain, we concatenated all 8-yr long time-series from 2000 to 2007 at  
230 different grid points into a long data array. This means each data array has, at least, the number of  
231 grids  $\times$  8-yr  $\times$  365-day  $\times$  TMI swath coverage rate ( $\sim 70\%$ ) data points.

## 232 **4. Results**

### 233 *a. Convective amplification and decay*

234 As in Inoue and Back (2015b), we first verify the idea of the convective amplification/decay  
235 phases defined by Eqs. 8a and 8b. In doing so, we plotted in Fig. 3, (a) changes of precipitation  
236 over two days, (b) probabilities of increase in precipitation, and (c) precipitation, as a function of  
237 the drying efficiency  $\Gamma - \Gamma_C$ . Because the phases of Eqs. 8a and 8b hold only when convection  
238 is active or  $\nabla \cdot \langle s\mathbf{v} \rangle$  is positive, we removed all the data points with  $\nabla \cdot \langle s\mathbf{v} \rangle$  less than  $50 \text{ Wm}^{-2}$   
239 in order to exclude convectively inactive times and to avoid division by zero. Furthermore, 2.5

240 % outliers from the left and right tails of the PDF of  $\Gamma - \Gamma_C$  were also removed to avoid biases  
 241 due to very large and small values of  $\Gamma - \Gamma_C$ . Those threshold values are arbitrary, and the results  
 242 shown are insensitive to them. In section 4c, we generalize this condition and investigate the whole  
 243 convective life-cycle.

244 Figure 3a, which shows precipitation changes as a function of  $\Gamma - \Gamma_C$ , was made as follows.  
 245 First, we sorted the data array of precipitation changes, computed with a centered difference over  
 246 two days, in accordance with the order of  $\Gamma - \Gamma_C$ , and all the data points corresponding to  $\nabla \cdot \langle s\mathbf{v} \rangle$   
 247 less than  $50 \text{ Wm}^{-2}$  and 2.5 % outliers of  $\Gamma - \Gamma_C$  were removed. That sorted data array was averaged  
 248 within 5-percentile bins of  $\Gamma - \Gamma_C$  to render Fig. 3a. Figure 3b, which illustrates probabilities of  
 249 increase in precipitation against  $\Gamma - \Gamma_C$ , was made similarly. We computed the ratio of the number  
 250 of events with positive precipitation changes to the total event number within the 5-percentile bins  
 251 of  $\Gamma - \Gamma_C$ .

252 Both Figs. 3a and 3b strongly support the hypothesis of the convective amplification/decay  
 253 phases. When the drying efficiency  $\Gamma - \Gamma_C$  is negative/positive, the precipitation amplifies/decays  
 254 in the next day (i.e., positive/negative precipitation changes) at high probability ( $\sim 80 \%$ ), and  
 255 when  $\Gamma - \Gamma_C$  changes its sign, the phase abruptly switches. This pattern is robust among all the  
 256 oceanic basins as shown with the lines in different colors.

257 When considering significant scatters in  $P$ -vs- $\langle q \rangle$  scatter plots in general, the assumption of the  
 258 positive correlation between  $P$  and  $\langle q \rangle$  in Eq. 4 seems to be an oversimplification. In spite of the  
 259 seemingly oversimplified assumption, the amplifying/decaying phases defined by  $\Gamma - \Gamma_C$  were far  
 260 more robust than we expected. This significant predictability is not obvious from scatter plots of  
 261  $P$ -vs- $\langle q \rangle$  in general.

262 Figure 3c illustrates precipitation as a function of  $\Gamma - \Gamma_C$ , rendered with the same binning method  
 263 as the others. In the amplifying phase (i.e.,  $\Gamma - \Gamma_C < 0$ ), the precipitation increases as  $\Gamma - \Gamma_C$  be-

comes less negative and reaches the maximum when  $\Gamma - \Gamma_C$  is zero, or  $\Gamma$  is equal to  $\Gamma_C$ ; in the decaying phase (i.e.,  $\Gamma - \Gamma_C > 0$ ), the precipitation decreases with increase in  $\Gamma - \Gamma_C$ . The occurrence of the maximum precipitation at  $\Gamma = \Gamma_C$  (or  $\Gamma - \Gamma_C = 0$ ) is rooted in the fact that the local maximum of precipitable water and precipitation happens when  $\partial \langle q \rangle / \partial t \simeq 0$ . The precipitation minimum also happens when  $\Gamma = \Gamma_C$ , but convectively inactive times were removed through the procedures described above.

In the next subsection, we show that  $\Gamma_C$  can be approximated as a constant in the satellite data used. This indicates that the phase of convection is determined by the criticality of the GMS (i.e., whether  $\Gamma$  is greater or less than some critical constant). This is why we refer to  $\Gamma_C$  as the critical GMS.

#### *b. Constancy of critical GMS*

Figure 4 shows scatter plots for the diabatic source ( $D \equiv \langle Q_R \rangle + S$ ) and divergence of column MSE ( $+\nabla \cdot \langle h\mathbf{v} \rangle$ ) as a function of divergence of column DSE ( $+\nabla \cdot \langle s\mathbf{v} \rangle$ ) over the four oceanic basins. The color shade represents the base-10 logarithm of the number of occurrences within  $12.5 \text{ Wm}^{-2} \times 25.0 \text{ Wm}^{-2}$  grids of  $D$  (or  $\nabla \cdot \langle h\mathbf{v} \rangle$ ) and  $\nabla \cdot \langle s\mathbf{v} \rangle$ . The black dashed line in each panel was computed with regression through the origin, and the gray line was computed with the binning average within  $200 \text{ Wm}^{-2}$ -wide bins of  $\nabla \cdot \langle s\mathbf{v} \rangle$ .

It can be seen in the left column of Fig. 4 that the scatter of  $D$  is concentrated along the regression line through the origin, and this pattern is similar among all the oceanic basins with slightly varying regression slopes. This linear trend of  $D$  appears to be robust especially when compared with the scatter of  $\nabla \cdot \langle h\mathbf{v} \rangle$  in the right column. Thus, we can approximate  $D$  as

$$D \simeq \gamma \nabla \cdot \langle s\mathbf{v} \rangle. \quad (15)$$

Strictly speaking,  $\gamma$  is not a constant, but slightly varies depending on the value of  $\nabla \cdot \langle s\mathbf{v} \rangle$  as depicted in the gray binned lines. But the regression lines capture well the overall trend of the scatter of  $D$ . Therefore, as proposed in section 2, we can approximate the critical GMS (Eq. 7) to be  $\gamma$ , which is a constant relevant to the characteristic GMS defined by Inoue and Back (2015b) that is discussed in section 4d.

Now we can replace  $\Gamma_C$  in the drying efficiency  $\Gamma - \Gamma_C$  with  $\gamma$ , and define the amplifying/decaying phases in terms of  $\Gamma - \gamma$  as Eqs. 9a and 9b: Negative/positive  $\Gamma - \gamma$  corresponds to the amplifying/decaying phase, respectively. Figure 5 verifies this idea, which was made in the same way as Fig. 3 but as a function of  $\Gamma - \gamma$  instead of  $\Gamma - \Gamma_C$ . This figure illustrates that  $\Gamma - \gamma$  works well to describe the convective amplification and decay phases among all the oceanic basins. Thus, we can claim that convection will most likely amplify/decay when  $\Gamma$  is less/greater than  $\gamma$  and the local maximum happens at  $\Gamma = \gamma$ . This means that, if the value of  $\gamma$  is given, the GMS is telling us about whether the convection is amplifying or decaying.

As discussed in sections 2 and 4a, the phase relationships in terms of  $\Gamma - \gamma$  hold only when  $\nabla \cdot \langle s\mathbf{v} \rangle$  is positive. Now we generalize this condition to include the whole convective life-cycle in the next subsection. This can be done by utilizing the linear trend in Eq. 15 and a diagnostic framework which we refer to as the GMS plane.

### c. GMS plane

By assuming the positive correlation between  $P$  and  $\langle q \rangle$  in Eq. 4 and the linear trend of  $D$  in Eq. 15, we can derive a simple model:

$$\frac{\partial P}{\partial t} \sim \frac{\partial \langle Lq \rangle}{\partial t} \simeq -\nabla \cdot \langle h\mathbf{v} \rangle + \gamma \nabla \cdot \langle s\mathbf{v} \rangle. \quad (16)$$



305 This model is a generalization of the amplifying/decaying phases in Eqs. 9a and 9b; when  $\nabla \cdot \langle s\mathbf{v} \rangle$   
306 is positive, we can divide this by  $\nabla \cdot \langle s\mathbf{v} \rangle$  and yield the same relationships as Eqs. 9a and 9b.

307 We bear out the validity of this simple model in Fig. 6, in which probabilities of increase in  
308 precipitation are plotted in the plane of  $\nabla \cdot \langle h\mathbf{v} \rangle$ -vs- $\nabla \cdot \langle s\mathbf{v} \rangle$  that we call the GMS plane<sup>3</sup>. In this  
309 plane, the tangent of an phase angle corresponds to the GMS. The probabilities were computed  
310 similarly to Fig. 3, but now within 2D bins instead of 1D bins. We computed the ratio of the  
311 number of events with positive precipitation changes over two days to the total event number  
312 within  $50 \text{ Wm}^{-2} \times 50 \text{ Wm}^{-2}$  bins of  $\nabla \cdot \langle h\mathbf{v} \rangle$  and  $\nabla \cdot \langle s\mathbf{v} \rangle$ . The regression lines through the origin  
313 and the binned lines are identical to those in the left column of Fig. 4. The slopes of the regression  
314 lines correspond to  $\gamma$ , which is the approximated critical GMS  $\Gamma_C$ .

315 It is clear in this figure that the grids below/above the critical line (or the regression line) exhibit  
316 high/low probabilities of convective amplification, and there is an abrupt transition near the critical  
317 line. This figure strongly supports the validity of the model in Eq. 16; the grids below/above the  
318 critical line correspond to positive/negative RHS of Eq. 16, thus to the amplification/decay of  
319 convection, respectively. Figure 6 is a generalized version of Fig. 3b.

320 This GMS plane is useful particularly because it acts like a phase plane. If a data point lies below  
321 the critical line, the convection will most likely intensify in the next day, thus the data point will  
322 move toward the right in the GMS plane; in contrast, a data point above the critical line will move  
323 toward the left. Furthermore, we know that precipitation reaches the maximum on the critical line  
324 (i.e.,  $\Gamma = \gamma$ ) from Fig. 5c. Thus, we expect that convective life-cycles in the GMS plane look  
325 like orbiting fluctuations around the critical line. This idea is illustrated in Fig. 7, which shows  
326 the mean values of temporal changes of  $\nabla \cdot \langle h\mathbf{v} \rangle$  and  $\nabla \cdot \langle s\mathbf{v} \rangle$  as arrows at each grid in the GMS

---

<sup>3</sup>Utilization of the GMS plane is not a new concept. For instance, some past studies analyzed scatter plots in the GMS plane (e.g., Raymond and Fuchs 2009; Benedict et al. 2014).

plane. The mean values were computed within  $100 \text{ Wm}^{-2} \times 100 \text{ Wm}^{-2}$  bins. This figure illustrates that the GMS plane is a phase plane in which each convective life-cycle tends to orbit around the critical GMS line. It should be noted that this phase plane behavior has been already claimed by Masunaga and L’Ecuyer (2014) and Inoue and Back (2015a), though not illustrated in this way.

Figure 7 is an alternative depiction of a GMS transition to plotting a time-series of it. In general, computation of the GMS becomes troublesome when its denominator is small. Depicting a GMS transition as a phase transition in the GMS plane can avoid the computational problem of the GMS, thus we can apply this methodology to the whole convective life-cycle.

Since the behaviors illustrated in Figs. 6 and 7 are robust among all the oceanic basins with slightly varying regression slopes, we plotted in Fig. 8 those for the whole oceanic regions where the mean precipitation is greater than 5 mm/day. The gray dashed and dotted lines in it represent the range of the geographic variability of a regression slope  $\gamma$ . This figure summarizes important aspects of the GMS: When considering  $\nabla \cdot \langle s\mathbf{v} \rangle > 0$  and  $\nabla \cdot \langle s\mathbf{v} \rangle < 0$  cases separately, values of the GMS (i.e., phase position in the GMS plane) have a capability to predict the subsequent convective evolution in a qualitative manner, and that law is quite universal throughout the whole tropical ocean. In the next subsection, we discuss the geographic variability of a regression slope  $\gamma$ , which is relevant to the characteristic GMS defined by Inoue and Back (2015b).

#### 344 *d. Characteristic GMS*

So far, we have discussed a time-dependent aspect of the GMS. Now let us discuss the quasi-time-independent “background GMS”, which we refer to as the characteristic GMS. In the following discussion, we clarify how to calculate a meaningful value of the background GMS.

In the previous sections, we introduced the critical GMS  $\gamma$ , calculated as a slope of a regression line through the origin, which represents a feedback between diabatic sources (column radiation

and surface fluxes) and convection. And we showed that  $\gamma$  corresponds to a value of the GMS at the convective maximum, which we denote  $\Gamma_{max}$ . In addition to those, Inoue and Back (2015b) listed three different calculations of the background GMS as follows:

1. GMS calculated from a scatter plot of anomalous  $\nabla \cdot \langle h\mathbf{v} \rangle$  against  $\nabla \cdot \langle s\mathbf{v} \rangle$ :

$$\tilde{\Gamma}' \equiv \frac{\overline{\nabla \cdot \langle h\mathbf{v} \rangle' * \nabla \cdot \langle s\mathbf{v} \rangle'}}{\overline{\nabla \cdot \langle s\mathbf{v} \rangle'^2}}, \quad (17)$$

2. GMS calculated from a scatter plot of non-anomalous  $\nabla \cdot \langle h\mathbf{v} \rangle$  against  $\nabla \cdot \langle s\mathbf{v} \rangle$ :

$$\tilde{\Gamma} \equiv \frac{\overline{\nabla \cdot \langle h\mathbf{v} \rangle * \nabla \cdot \langle s\mathbf{v} \rangle}}{\overline{\nabla \cdot \langle s\mathbf{v} \rangle^2}}, \quad (18)$$

and

3. Climatological GMS:

$$\bar{\Gamma} \equiv \frac{\overline{\nabla \cdot \langle h\mathbf{v} \rangle}}{\overline{\nabla \cdot \langle s\mathbf{v} \rangle}}, \quad (19)$$

where the bar represents a time average and the prime represents departure from the time average. Thus, as total, we have five different ways of calculations of the background GMS ( $\gamma$ ,  $\Gamma_{max}$ ,  $\tilde{\Gamma}'$ ,  $\tilde{\Gamma}$ , and  $\bar{\Gamma}$ ), and Inoue and Back (2015b) claimed that all of them are close to each other so that they can be used interchangeably. They are collectively called the characteristic GMS. In the discussion below, we show that all versions of the characteristic GMS are close to each other over the whole tropical ocean except for the climatological GMS  $\bar{\Gamma}$ , which is so sensitive to data errors that it should not be used as a diagnostic tool.

Figure 9 shows the geographic variability of (a) the critical GMS  $\gamma$ , (b) the anomalous characteristic GMS  $\tilde{\Gamma}'$ , (c) the non-anomalous characteristic GMS  $\tilde{\Gamma}$ , and (d) the climatological GMS  $\bar{\Gamma}$  over the oceanic regions where the mean precipitation is greater than 5 mm/day. The first three panels [(a)–(c)] exhibit similar geographic patterns; the values are slightly higher in the Indian and the western Pacific Oceans than in the central-eastern Pacific and the Atlantic Oceans. The

369 correlations of the spatial pattern of Fig. 9a with Figs. 9b and c are 0.848 and 0.737, respectively.  
 370 It should be noted that the color scales in Figs. 9b and c are shifted by 0.01 compared with that in  
 371 Fig. 9a. That small departure is due to nonzero covariance between  $\partial\langle q\rangle/\partial t$  and  $\nabla\cdot\langle\mathbf{sv}\rangle$  owing to  
 372 slight lags between  $P$  and  $\langle q\rangle$  (see section 5 in Inoue and Back 2015b).

373 The geographic patterns shown are, to some extent, consistent with the geographic variability  
 374 of vertical velocity profiles. In general, vertical-velocity-profile shapes are top-heavier (associ-  
 375 ated with greater GMS) in the Indian and the western Pacific Oceans with weak SST gradient,  
 376 and bottom-heavier (associated with smaller GMS) in the central-eastern Pacific and the Atlantic  
 377 Oceans with strong SST gradient (e.g., Back and Bretherton 2006; Sobel and Neelin 2006; Back  
 378 and Bretherton 2009a,b; Back et al. 2016). But it should be noted that the definitions of the char-  
 379 acteristic GMS used here include both the horizontal and vertical components of the GMS, and  
 380 thus their values cannot be determined solely by vertical velocity profiles. It would be interesting  
 381 to investigate further the mechanisms which control the geographic patterns of the characteristic  
 382 GMS.

383 Although the values of the three characteristic GMSs,  $\gamma$ ,  $\tilde{\Gamma}'$ , and  $\tilde{\Gamma}$ , are consistent with each other,  
 384 the climatological GMS  $\bar{\Gamma}$  exhibits a quite different geographic pattern as depicted in Fig. 9d. It  
 385 shows that  $\bar{\Gamma}$  is negative in the eastern Pacific and the Atlantic Oceans and the color scale is far  
 386 different from those in the other panels. We claim that this significant discrepancy is due to the  
 387 sensitivity of this metric to data errors. In Fig. 4, the mean values of  $(\nabla\cdot\langle h\mathbf{v}\rangle, \nabla\cdot\langle\mathbf{sv}\rangle)$  are plotted  
 388 with the blue cross-marks. The values of those are  $(19.3 \text{ Wm}^{-2}, 118.0 \text{ Wm}^{-2})$ ,  $(15.3 \text{ Wm}^{-2}, 174.9$   
 389  $\text{Wm}^{-2})$ ,  $(-2.1 \text{ Wm}^{-2}, 120.9 \text{ Wm}^{-2})$ , and  $(-5.9 \text{ Wm}^{-2}, 107.1 \text{ Wm}^{-2})$ , respectively, for IO, WP, EP,  
 390 and AO. One can notice that the numerator of  $\bar{\Gamma}$ ,  $\overline{\nabla\cdot\langle h\mathbf{v}\rangle}$ , is a tiny number especially in EP and  
 391 AO. Thus even a few  $\text{Wm}^{-2}$  of its errors can cause crucial errors in  $\bar{\Gamma}$  with a sign flip. Therefore,  
 392 we conclude that the metric of the climatological GMS  $\bar{\Gamma}$  is so sensitive to data errors that it should

not be used as a diagnostic tool especially with observational data involving non-negligible biases. Recently, the GMS is used as a diagnostic tool for the inter-model comparison (e.g., Benedict et al. 2014; Hannah and Maloney 2014; Maloney et al. 2014). Due to the issues with the climatological GMS, it would be useful to use the versions of the characteristic GMS calculated from a scatter plot for this type of analysis in the future.

*e. GMS transitions during DYNAMO*

Lastly, we briefly show the GMS transitions on the MJO time-scale. In doing so, we plotted in the GMS plane the transitions of different MJO events during the DYNAMO field campaign. We used version 3a of the Colorado State University quality controlled observations from the DYNAMO field campaign (Johnson and Ciesielski 2013; Ciesielski et al. 2014a,b; Johnson et al. 2015). All the variables plotted are averages over the northern sounding array and also 10-day running averages.

There were three MJO events during the DYNAMO period, which are depicted in the different colors (red, green, and blue) in Fig. 10. Figure 10a is a time-series of precipitation rate. The temporal transitions are depicted as the gradation of the colors. For those MJO events, the temporal transitions are also plotted in the GMS plane (Fig. 10b). This is an alternative illustration of GMS transitions to those given by Sobel et al. (2014) and Sentić et al. (2015).

The first and second MJO events shown in the reddish and greenish colors behave consistently with the phase plane behavior discussed in section 4c. Each convective life-cycle orbits counter-clockwise around the characteristic GMS line, calculated with Eq. 17, depicted as the gray line. The third MJO event in the bluish color behaves slightly differently from the first two MJO events in such a way that the slope of the orbit axis is steeper than the critical GMS. This result might

415 imply that different MJO events have different values of the critical or the characteristic GMS, and  
416 it might be interesting to study how those are regulated.

## 417 **5. Discussion**

### 418 *a. Applicability of the GMS plane analysis*

419 The results shown in this study are based on the four simple assumptions:

- 420 1. MSE budgets are closed.
- 421 2. Column-integrated DSE anomalies are much smaller than precipitable water anomalies.
- 422 3. Precipitation is positively correlated with precipitable water.
- 423 4. The diabatic source terms can be approximated in a linear form with respect to the divergence  
424 of column DSE (or precipitation).

425 The second assumption doesn't rule out the possibility that small temperature anomalies play  
426 crucial roles in the dynamics. This second assumption is likely valid only on time-scales longer  
427 than a day (e.g., Inoue and Back 2015b). One would need to test the extent to which assumptions  
428 1, 2, and 4 are valid in tropical cyclones.

429 As long as those assumptions are satisfied, the GMS phase transitions shown in Figs. 6 and 7  
430 hold. The first three assumptions are generally well verified in the tropics<sup>4</sup>. The validity of the  
431 last assumption, which is rooted in the linear feedbacks of the cloud-radiation and the convection-  
432 evaporation, is partially less certain than the others. The cloud-radiation feedback has been well  
433 verified in the past observational studies (e.g., Lin and Mapes 2004; Inoue and Back 2015a; John-  
434 son et al. 2015) and implemented in many theoretical models (Sobel and Gildor 2003; Fuchs and

---

<sup>4</sup>Tropical cyclones might be the exception for the assumptions. For investigating them, the moist entropy budget could be a better choice as demonstrated by Juračić and Raymond (2016).

Raymond 2002, and many others). In contrast, the mechanism of the convection-evaporation feedback is not well understood although observational studies suggested its existence (e.g., Back and Bretherton 2005). Nevertheless, both the current study and the study by Inoue and Back (2015b) with the TOGA COARE field campaign data seem to bear out the validity of the fourth assumption.

Therefore, we believe that the GMS plane analysis has a wide range of applicability, including analyses of convectively coupled equatorial waves (CCEWs) and MJO life-cycles. Another benefit of this analysis is that it is applicable to all kinds of data, involving satellite, reanalysis, field campaign data, and outputs of numerical models. Thus we expect it will provide us with a standard framework for diagnostics of tropical convective disturbances.

*b. Two aspects of GMS analysis: time-dependent and quasi-time-independent aspects*

The GMS can be studied in two ways: as a phase transition in the GMS plane, and as the characteristic GMS. The former is highly time-dependent and the latter corresponds to quasi-time-independent background GMS. This study demonstrated how to assess those different aspects separately. The transitions of time-dependent GMS can be visualized in the GMS plane as an orbiting fluctuation around the background GMS line. And the background GMS varies among different geographic locations.

These two aspects of the GMS tell us about how we should interpret the GMS in theoretical studies, which is given as a constant (Fuchs and Raymond 2002; Sobel and Maloney 2013; Adames and Kim 2016, among many others). In order to clarify that, we point out two important caveats of GMS analyses:

1. Physical interpretations of the GMS are different depending on how to compute it.
2. The characteristic GMS is the GMS associated with the moisture-mode theories.

457 The GMS can be calculated in various ways. For instance, we can take a ratio of spatially averaged  
 458  $\nabla \cdot \langle h\mathbf{v} \rangle$  to spatially averaged  $\nabla \cdot \langle s\mathbf{v} \rangle$  to get a local value of the GMS (e.g., Masunaga and L'Ecuyer  
 459 2014; Sobel et al. 2014; Inoue and Back 2015b; Sentić et al. 2015). On the other hand, we can  
 460 compute the GMS from a scatter-plot as in section 4d and some past studies (e.g., Raymond and  
 461 Fuchs 2009; Benedict et al. 2014). In the discussion below, we demonstrate that those two versions  
 462 of the GMS have distinct physical interpretations, and that the GMS relevant to the moisture-mode  
 463 theories is the one calculated from a scatter-plot.

464 For proceeding with the discussion, we crudely summarize the moisture-mode theory, ignoring  
 465 some details. The model of the linear moisture mode can be expressed as

$$\frac{\partial P'}{\partial t} = - \left[ \Gamma_{\text{eff},r} + i\Gamma_{\text{eff},i} \right] P', \quad (20)$$

466 where  $P'$  is a precipitation anomaly, and the real component  $\Gamma_{\text{eff},r}$  and the imaginary component  
 467  $\Gamma_{\text{eff},i}$  are determined by the model parameters. The choice of these notations implies that they are  
 468 associated with (but not equivalent to) the effective GMS<sup>5</sup>. The minus sign is there for consistency  
 469 with the past literature.

470 We assume  $P'$  has the form

$$P'(x, t) = \hat{P} \exp [ikx + (\sigma_r + i\sigma_i)t], \quad (21)$$

471 where  $\hat{P}$  is an amplitude,  $k$  is a zonal wavenumber,  $\sigma_r$  and  $\sigma_i$  are real and imaginary frequencies  
 472 respectively. Plugging Eq. 21 into Eq. 20 yields  $\sigma_r = -\Gamma_{\text{eff},r}$  and  $\sigma_i = -\Gamma_{\text{eff},i}$ . Thus, when  $\Gamma_{\text{eff},r}$   
 473 is negative, the mode is destabilized ( $\sigma_r > 0$ );  $\Gamma_{\text{eff},i}$  is associated with the wave propagation. In  
 474 the moisture-mode models,  $\Gamma_{\text{eff},r}$  is close to the effective GMS, indicating the effectively negative

---

<sup>5</sup>The definition of the effective GMS differs among different literature. Some includes horizontal MSE advection in the definition (e.g., Adames and Kim 2016; Sakaeda and Roundy 2016) and the other includes surface evaporation in it (e.g., Hannah and Maloney 2014; Sakaeda and Roundy 2016).  $\Gamma_{\text{eff},r}$  here is the closest to the “projected total effective GMS” in Adames and Kim (2016).



475 GMS is necessary for the destabilization of the moisture mode [see Adames and Kim (2016),  
 476 which is the closest to our argument here].

477 The model parameters,  $\Gamma_{\text{eff},r}$  and  $\Gamma_{\text{eff},i}$ , consist of the parametrization of four different compo-  
 478 nents: horizontal MSE advection, vertical MSE advection, radiative heating, and surface fluxes.  
 479 For elucidating the behavior of the GMS, let's focus on the advective term, ignoring the horizontal  
 480 advection for simplicity. The argument below can be extended to include other terms.

481 In the context of a linear model, we can express the column-integrated vertical MSE advection  
 482 as

$$\langle \omega \partial h / \partial p \rangle' = \left[ \Gamma_{v,r} + i \Gamma_{v,i} \right] P', \quad (22)$$

483 where  $\omega$  is vertical pressure velocity;  $\Gamma_{v,r}$  and  $\Gamma_{v,i}$  are model parameters.  $\Gamma_{v,r}$  contributes to  
 484 the stability of the system (i.e.,  $\Gamma_{\text{eff},r} = \Gamma_{v,r} + \text{other terms}$ );  $\Gamma_{v,i}$  represents the contribution of  
 485 the vertical MSE advection to the propagation (i.e.,  $\Gamma_{\text{eff},i} = \Gamma_{v,i} + \text{other terms}$ ), which might be  
 486 parametrized as frictionally induced moisture convergence or vertical advection by bottom-heavy  
 487  $\omega$  [see Eq. (12) in Sobel and Maloney (2013) or Eq. (4a) in Adames and Kim (2016)].  $\Gamma_{v,r}$ , which  
 488 is set to be a constant parameter, corresponds to the (vertical) GMS in the theoretical work. Now  
 489 let's visualize the temporal transitions of  $\langle \omega \partial h / \partial p \rangle'$  and  $P'$  expressed by Eqs. 20, 21 and 22 as in  
 490 Fig. 10.

491 Since this study investigated the MSE budget in Eulerian columns at fixed locations, we can  
 492 set  $x = 0$  in Eq. 21 without loss of generality. Because only the real component of Eq. 22 makes  
 493 physical sense, plugging Eq. 21 into Eq. 22 and extracting the real component yields

$$\langle \omega \partial h / \partial p \rangle' = \hat{P} \exp \left( -\Gamma_{\text{eff},r} t \right) \left[ \Gamma_{v,r} \cos \left( \Gamma_{\text{eff},i} t \right) + \Gamma_{v,i} \sin \left( \Gamma_{\text{eff},i} t \right) \right], \quad (23)$$

where we set  $\sigma_r = -\Gamma_{\text{eff},r}$  and  $\sigma_i = -\Gamma_{\text{eff},i}$ , and we assume  $\hat{P}$  is a real number. Similarly, the real components of  $P'$  and  $\partial P'/\partial t$  are expressed as

$$P' = \hat{P} \exp\left(-\Gamma_{\text{eff},r}t\right) \cos\left(\Gamma_{\text{eff},i}t\right), \quad (24)$$

$$\frac{\partial P'}{\partial t} = \hat{P} \exp\left(-\Gamma_{\text{eff},r}t\right) \left[-\Gamma_{\text{eff},r} \cos\left(\Gamma_{\text{eff},i}t\right) - \Gamma_{\text{eff},i} \sin\left(\Gamma_{\text{eff},i}t\right)\right]. \quad (25)$$

Now we want to estimate the values of  $\Gamma_{v,r}$  and  $\Gamma_{v,i}$  from observations in order to visualize the transitions of Eqs. 23 and 24. First, in a long time-series, we can approximate  $\Gamma_{\text{eff},r} \simeq 0$  otherwise the precipitation grows infinitely or converges to zero. Therefore, we can write Eqs. 23, 24, and 25 as

$$\langle \omega \partial h / \partial p \rangle' \simeq \hat{P} \left[ \Gamma_{v,r} \cos\left(\Gamma_{\text{eff},i}t\right) + \Gamma_{v,i} \sin\left(\Gamma_{\text{eff},i}t\right) \right], \quad (26)$$

$$P' \simeq \hat{P} \cos\left(\Gamma_{\text{eff},i}t\right), \quad (27)$$

$$\frac{\partial P'}{\partial t} \simeq -\hat{P} \Gamma_{\text{eff},i} \sin\left(\Gamma_{\text{eff},i}t\right). \quad (28)$$

For estimating  $\Gamma_{v,r}$ , we want to multiply Eq. 26 with Eq. 27 and take an integration with respect to time from 0 to  $2\pi$ . In such a way,  $\Gamma_{v,r}$  can be estimated in observational data as

$$\Gamma_{v,r} \simeq \frac{\overline{\langle \omega \partial h / \partial p \rangle' * P'}}{\overline{P'^2}}, \quad (29)$$

where the bar, which represents a time average, can be considered as an integration from 0 to  $2\pi$  if a time-series is long enough. This is similar to the characteristic GMS defined by Eq. 17, indicating that  $\Gamma_{v,r}$ , which is relevant to the moisture-mode instability, can be estimated as the characteristic GMS. Similarly, we can estimate  $\Gamma_{v,i}$  as

$$\Gamma_{v,i} \simeq -\Gamma_{\text{eff},i} * \frac{\overline{\langle \omega \partial h / \partial p \rangle' * \partial P' / \partial t}}{\overline{(\partial P' / \partial t)^2}}. \quad (30)$$

Similar (but not the same) methods were used by Andersen and Kuang (2011) to compute the contributions of each MSE budget term to the stabilization and to the propagation of the MJO-like variability.

For a demonstration, we set the frequency to be  $\Gamma_{\text{eff},i} = 2\pi/40$  (day<sup>-1</sup>). Using the TOGA COARE data (the data description is presented in Appendix), we estimated  $\Gamma_{v,r}$  to be  $\sim 0.25$  and  $\Gamma_{v,i}$  to be  $\sim 0.05$ . But for the illustrative purpose, we used  $\Gamma_{v,i} = 0.15$  instead of 0.05. Using these values of the parameters, the temporal evolutions of Eqs. 23 and 24 are plotted in Fig. 11. Figure 11a illustrates a 40-day cycle of  $\langle \omega \partial h / \partial p \rangle'$  versus  $P'$  in the neutral condition (i.e.,  $\Gamma_{\text{eff},r} = 0$ ). This neutral condition occurs when the radiative feedback and surface flux feedback effects are balanced by the GMS (or  $\Gamma_{v,r}$ ). The cycle starts from the red dot, goes around counter-clockwise, and terminates at the blue dot. This behavior is consistent with that shown in the GMS plane in Figs. 7 and 10.

This figure clarifies why the GMS is a vexing quantity. From this figure, we can calculate two distinct values of the GMS:

$$\text{GMS (background)} \sim \Gamma_{v,r}, \quad (31)$$

$$\text{GMS (time-dependent)} \sim \Gamma_{v,r} + \Gamma_{v,i} \tan(\Gamma_{\text{eff},i} t), \quad (32)$$

where the former represents the slope of the major axis of the elliptic trajectory, which is calculated by Eq. 29; and the latter was computed by simply dividing Eq. 23 by Eq. 24. When we compute the GMS as a time-dependent quantity using time-series, it corresponds to Eq. 32. This time-dependent GMS can easily become negative, but that negative GMS is not relevant to the stability of the moisture mode; only  $\Gamma_{v,r}$  is associated with the stability.

Figures 11b illustrates the GMS plane behavior in an unstable condition where the effective GMS is set to be slightly negative ( $\Gamma_{\text{eff},r} = -0.01$ ). This condition occurs when the radiative feedback and surface flux feedback effects exceed the background GMS. There is a growing spiral due to an exponentially amplifying oscillation, which is a characteristic of destabilized linear

533 waves. In the real world, however, this kind of growing spiral is not expected to happen because  
534 nonlinear effects generally keep a disturbance from growing infinitely.

535 The distinction between the two versions of the GMS defined in Eqs. 31 and 32 becomes crucial  
536 when the size of an observational domain is smaller than that of a MJO envelope. In such a case,  
537 the contribution of the MSE advection to the propagation (i.e., nonzero  $\Gamma_{v,i}$ ) easily makes the  
538 time-dependent GMS negative via Eq. 32. But that negative GMS must not be confused with the  
539 negative background GMS for the destabilization.

540 In the same sense, the drying efficiency calculated in this study is not the same as the effective  
541 GMS used in the past theoretical literature. This distinction cannot be emphasized too much  
542 because the terminology “GMS” is now used to mean both the time-dependent and the background  
543 ones. It is crucial to keep in mind that those two quantities must be interpreted differently: the  
544 quasi-time-independent GMS represents the stability of the background condition, and thus is  
545 relevant to the moisture mode. On the other hand, the highly time-dependent GMS does not  
546 represent the background stability, but it represents “advective drying efficiency” via convectively  
547 induced large-scale circulations, which expresses local favorability for convection due to large-  
548 scale circulations.

## 549 **6. Concluding remarks**

550 We investigated the gross moist stability (GMS) and its related quantities utilizing satellite-based  
551 products over the tropical ocean. In the data sets used, we found the diabatic source, which is  
552 the combination of column radiation and surface fluxes, can be expressed as a linear function  
553 of the divergence of column moist static energy (MSE) with a slope of  $\gamma$ , which we call the  
554 critical GMS. This linear relationship, together with a positive correlation between precipitation  
555 and precipitable water, indicates that when the GMS is less/greater than the critical GMS the

556 convection amplifies/decays. This means that, if the value of the critical GMS is given, values  
557 of the GMS tell us whether the convection will amplify or decay. This statement is, however,  
558 only true when the denominator of the GMS, the divergence of column dry static energy (DSE), is  
559 positive. We generalized this condition by introducing the “GMS plane” analysis.

560 We refer to the plane of the divergence of column MSE against the divergence of column DSE  
561 as the GMS plane. In this plane, we can easily determine whether convection is in the amplifying  
562 phase or in the decaying phase. First, we draw a line going through the origin whose slope is  
563 the critical GMS. Then, if a data point lies below/above the critical line, the convection is most  
564 likely in the amplifying/decaying phase. Furthermore, the GMS plane behaves as a phase plane  
565 in which each convective life-cycle seems like an orbiting fluctuation around the critical GMS  
566 line. We found that the GMS plane behavior is consistent even on the MJO time-scale. This  
567 GMS plane behavior indicates that values of the GMS (or phase positions in the GMS plane)  
568 qualitatively predict the subsequent convective evolution. This property is theoretically important  
569 because it means we can deduce future information from the pair of the divergence of MSE and  
570 the divergence of DSE, which are both diagnostic quantities instead of prognostic quantities.

571 This study demonstrates that the GMS analyses have two different aspects: time-dependent and  
572 quasi-time-independent aspects. The GMS can be calculated both as a highly time-dependent  
573 quantity and as a quasi-time-independent quantity. And we can visualize those two different as-  
574 pects in the GMS plane; the transitions of time-dependent GMS can be depicted in the GMS  
575 plane as an orbiting fluctuation around the quasi-time-independent GMS line. We emphasized that  
576 those two must be interpreted differently. The time-dependent GMS represents “advective drying  
577 efficiency”, which expresses local favorability for convection. On the other hand, the quasi-time-  
578 independent GMS represents the stability of the background condition and it is the GMS relevant  
579 to moisture-mode theories.

580 We listed different calculations of the quasi-time-independent GMS: (i) a regression slope from a  
581 scatter plot, and (ii) the ratio of climatological MSE divergence to climatological DSE divergence.  
582 The former GMS exhibits robust geographic patterns; the values are slightly higher in the Indian  
583 and the western Pacific Oceans than in the central-eastern Pacific and the Atlantic Oceans. The  
584 latter climatological GMS turns out to be so sensitive to data errors that we concluded that it should  
585 not be used as a diagnostic tool.

586 *Acknowledgments.* Influential conversations with Hirohiko Masunaga shaped the direction this  
587 project took. Figure 7 in this study was suggested by Christopher Bretherton. Very insightful  
588 reviews by Adam Sobel, David Raymond, and Walter Hannah significantly improved our first  
589 draft. We thank Jesse Stroik for his technical support. We also thank Tristan L'Ecuyer and William  
590 Olson for the radiative heating data, Richard Johnson and Paul Ciesielski for the DYNAMO data,  
591 and Minghua Zhang for the TOGA COARE data. The first author thanks Daniel Vimont, Gregory  
592 Tripoli, Matthew Hitchman, and Samuel Stechmann for the comments for his PhD thesis, which  
593 partially contributes to this paper. This research is supported by NASA Grant NNX12AL96G and  
594 NSF Grant MSN188169.

## 595 APPENDIX

### 596 **Underestimation of characteristic GMS with satellite data**

597 In order to check the reliability of the values of the characteristic GMSs computed with the satellite  
598 data, we compared those to the values computed with field campaign data. Two field campaign  
599 data sets were investigated: (i) the TOGA COARE field campaign data constructed by Minghua  
600 Zhang with an objective scheme called the constrained variational analysis (Zhang and Lin 1997),  
601 and (ii) the DYNAMO field campaign data used in section 4e.

Three characteristic GMSs,  $\tilde{\Gamma}'$ ,  $\tilde{\Gamma}$ , and  $\gamma$  were computed using both the field campaign data sets and the satellite data in the same regions, and compared with each other. It should be noted that there are no overlaps of the observational time periods; the TOGA COARE and DYNAMO field campaigns were conducted, respectively, from 1 November 1992 to 28 February 1993, and from 1 October to 31 December 2011, and the satellite data used here is from 1 January 2000 to 31 December 2007. This inter-comparison is implicitly dependent on the assumption that the characteristic GMSs are quasi-time-independent in the ITCZ.

Another important note is that the surface flux data in the TOGA COARE and DYNAMO data sets were derived in different ways. During TOGA COARE, the surface meteorology was collected from a buoy moored near the center of the domain (Weller and Anderson 1996) whereas the surface flux data during DYNAMO were obtained from TropFlux (Kumar et al. 2011) whose surface meteorology was derived from the corrected ERA-Interim. Discussion about the differences of those data sets is beyond the scope of this study. In this study, we simply assumed the field campaign data as the “true” data with which the satellite estimates are compared. But it should be noted that Hannah et al. (2016) demonstrated that the field campaign sounding array is sometime inaccurate due to sparse sampling stations that provide inaccurate horizontal gradients of moisture.

The values of the characteristic GMSs are summarized in Table A1<sup>6</sup>. Roughly speaking, the values of the different characteristic GMSs are consistent with each other as claimed in section 4d. The table shows that the satellite-based ones are approximately half of those computed with the field campaign data. This result indicates that the characteristic GMSs shown in Fig. 9 might be underestimated.

However, this underestimation does not change the general conclusions presented in this study; for instance, the underestimated characteristic GMS changes the slopes in Fig. 4, but the behavior

---

<sup>6</sup>The value of the critical GMS for DYNAMO in the table is slightly lower than that given in Fig. 10 because of a 10-day running average.

625 of the GMS plane discussed in section 4c is still valid. This was verified using the ERA-interim  
626 (not shown here).

627 It should be briefly noted that the values of the characteristic GMSs for DYNAMO are smaller  
628 than those given by Sentić et al. (2015), who used the same data as ours. This is simply because  
629 they computed the GMS with moist/dry entropy instead of moist/dry static energy. Generally, the  
630 GMSs computed with those different metrics exhibit different values, thus should not be compared  
631 with each other.



## References

- Adames, Á. F., and D. Kim, 2016: The MJO as a Dispersive, Convectively Coupled Moisture Wave: Theory and Observations. *J. Atmos. Sci.*, **73**, 913–941, doi:10.1175/JAS-D-15-0170.1.
- Andersen, J. A., and Z. Kuang, 2011: Moist static energy budget of MJO-like disturbances in the atmosphere of a zonally symmetric aquaplanet. *J. Climate*, **25**, 2782–2804, doi:10.1175/JCLI-D-11-00168.1.
- Back, L. E., and C. S. Bretherton, 2005: The relationship between wind speed and precipitation in the pacific ITCZ. *J. Climate*, **18**, 4317–4328, doi:10.1175/JCLI3519.1.
- Back, L. E., and C. S. Bretherton, 2006: Geographic variability in the export of moist static energy and vertical motion profiles in the tropical Pacific. *Geophys. Res. Lett.*, **33**, L17 810, doi:10.1029/2006GL026672.
- Back, L. E., and C. S. Bretherton, 2009a: On the Relationship between SST Gradients, Boundary Layer Winds, and Convergence over the Tropical Oceans. *J. Climate*, **22**, 4182–4196, doi:10.1175/2009JCLI2392.1.
- Back, L. E., and C. S. Bretherton, 2009b: A Simple Model of Climatological Rainfall and Vertical Motion Patterns over the Tropical Oceans. *J. Climate*, **22**, 6477–6497, doi:10.1175/2009JCLI2393.1.
- Back, L. E., Z. R. Hansen, and Z. J. Handlos, 2016: Estimating Vertical Motion Profile Top-heaviness: Reanalysis Compared to Satellite-based Observations and Stratiform Rain Fraction. *J. Atmos. Sci.*, accepted.

652 Benedict, J. J., E. D. Maloney, A. H. Sobel, and D. M. W. Frierson, 2014: Gross moist stability  
653 and MJO simulation skill in three full-physics GCMs. *J. Atmos. Sci.*, **71**, 3327–3349, doi:10.  
654 1175/JAS-D-13-0240.1.

655 Bretherton, C. S., M. E. Peters, and L. E. Back, 2004: Relationships between water vapor path and  
656 precipitation over the tropical oceans. *J. Climate*, **17**, 1517–1528, doi:10.1175/1520-0442(2004)  
657 017<1517:RBWVPA>2.0.CO;2.

658 Bretherton, C. S., and P. K. Smolarkiewicz, 1989: Gravity waves, compensating subsidence and  
659 detrainment around cumulus clouds. *J. Atmos. Sci.*, **46**, 740–759, doi:10.1175/1520-0469(1989)  
660 046<0740:GWCSAD>2.0.CO;2.

661 Bretherton, C. S., and A. H. Sobel, 2002: A Simple Model of a Convectively Coupled Walker  
662 Circulation Using the Weak Temperature Gradient Approximation. *J. Climate*, **15**, 2907–2920,  
663 doi:10.1175/1520-0442(2002)015<2907:ASMOAC>2.0.CO;2.

664 Charney, J. G., 1963: A note on large-scale motions in the tropics. *J. Atmos. Sci.*, **20**, 607–609,  
665 doi:10.1175/1520-0469(1963)020<0607:ANOLSM>2.0.CO;2.

666 Ciesielski, P. E., R. H. Johnson, K. Yoneyama, and R. K. Taft, 2014a: Mitigation of Sri Lanka  
667 Island Effects in Colombo Sounding Data and Its Impact on DYNAMO Analyses. *J. Meteor.*  
668 *Soc. Japan*, **92**, 385–405, doi:10.2151/jmsj.2014-407.

669 Ciesielski, P. E., and Coauthors, 2014b: Quality-Controlled Upper-Air Sounding Dataset for DY-  
670 NAMO/CINDY/AMIE: Development and Corrections. *Journal of Atmospheric and Oceanic*  
671 *Technology*, **31**, 741–764, doi:10.1175/JTECH-D-13-00165.1.

672 Curry, J. A., and Coauthors, 2004: Seaflux. *Bull. Amer. Meteor. Soc.*, **85**, 409–424, doi:10.1175/  
673 BAMS-85-3-409.

Dee, D. P., and Coauthors, 2011: The ERA-Interim reanalysis: configuration and performance of the data assimilation system. *Quart. J. Roy. Meteor. Soc.*, **137**, 553–597, doi:10.1002/qj.828.

Fuchs, Ž., and D. J. Raymond, 2002: Large-Scale Modes of a Nonrotating Atmosphere with Water Vapor and Cloud-Radiation Feedbacks. *J. Atmos. Sci.*, **59**, 1669–1679, doi:10.1175/1520-0469(2002)059<1669:LSMOAN>2.0.CO;2.

Fuchs, Ž., and D. J. Raymond, 2005: Large-Scale Modes in a Rotating Atmosphere with Radiative-Convective Instability and WISHE. *J. Atmos. Sci.*, **62**, 4084–4094, doi:10.1175/JAS3582.1.

Fuchs, Ž., and D. J. Raymond, 2007: A simple, vertically resolved model of tropical disturbances with a humidity closure. *Tellus A*, **59**, 344–354, doi:10.1111/j.1600-0870.2007.00230.x.

Hannah, W. M., and E. D. Maloney, 2014: The moist static energy budget in NCAR CAM5 hindcasts during DYNAMO. *J. Adv. Model. Earth Syst.*, **6**, 420–440, doi:10.1002/2013MS000272.

Hannah, W. M., B. E. Mapes, and G. S. Elsaesser, 2016: A Lagrangian View of Moisture Dynamics during DYNAMO. *J. Atmos. Sci.*, **73**, 1967–1985, doi:10.1175/JAS-D-15-0243.1.

Huffman, G. J., R. F. Adler, D. T. Bolvin, and E. J. Nelkin, 2010: The TRMM Multi-Satellite Precipitation Analysis (TMPA). *Satellite Rainfall Applications for Surface Hydrology*, M. Gebremichael, and F. Hossain, Eds., Springer Netherlands, 3–22.

Huffman, G. J., and Coauthors, 2007: The TRMM Multisatellite Precipitation Analysis (TMPA): Quasi-Global, Multiyear, Combined-Sensor Precipitation Estimates at Fine Scales. *J. Hydrometeor.*, **8**, 38–55, doi:10.1175/JHM560.1.

694 Inoue, K., and L. Back, 2015a: Column-Integrated Moist Static Energy Budget Analysis on  
695 Various Time Scales during TOGA COARE. *J. Atmos. Sci.*, **72**, 1856–1871, doi:10.1175/  
696 JAS-D-14-0249.1.

697 Inoue, K., and L. E. Back, 2015b: Gross Moist Stability Assessment during TOGA COARE:  
698 Various Interpretations of Gross Moist Stability. *J. Atmos. Sci.*, **72**, 4148–4166, doi:10.1175/  
699 JAS-D-15-0092.1.

700 Johnson, R. H., and P. E. Ciesielski, 2013: Structure and Properties of Madden-Julian Os-  
701 cillations Deduced from DYNAMO Sounding Arrays. *J. Atmos. Sci.*, **70**, 3157–3179, doi:  
702 10.1175/JAS-D-13-065.1.

703 Johnson, R. H., P. E. Ciesielski, J. H. Ruppert, and M. Katsumata, 2015: Sounding-Based Thermo-  
704 dynamic Budgets for DYNAMO. *J. Atmos. Sci.*, **72**, 598–622, doi:10.1175/JAS-D-14-0202.1.

705 Juračić, A., and D. J. Raymond, 2016: The effects of moist entropy and moisture budgets on  
706 tropical cyclone development. *J. Geophys. Res. Atmos.*, **121**, 2016JD025 065, doi:10.1002/  
707 2016JD025065.

708 Kumar, B. P., J. Vialard, M. Lengaigne, V. S. N. Murty, and M. J. McPhaden, 2011: TropFlux:  
709 air-sea fluxes for the global tropical oceans-description and evaluation. *Climate Dyn.*, **38**, 1521–  
710 1543, doi:10.1007/s00382-011-1115-0.

711 L’Ecuyer, T. S., and G. L. Stephens, 2003: The Tropical Oceanic Energy Budget from the  
712 TRMM Perspective. Part I: Algorithm and Uncertainties. *J. Climate*, **16**, 1967–1985, doi:  
713 10.1175/1520-0442(2003)016<1967:TTOEBF>2.0.CO;2.

714 L’Ecuyer, T. S., and G. L. Stephens, 2007: The Tropical Atmospheric Energy Budget from the  
715 TRMM Perspective. Part II: Evaluating GCM Representations of the Sensitivity of Regional

716 Energy and Water Cycles to the 1998-99 ENSO Cycle. *J. Climate*, **20**, 4548–4571, doi:10.1175/  
717 JCLI4207.1.

718 Lin, J.-L., and B. E. Mapes, 2004: Radiation Budget of the Tropical Intraseasonal Oscillation. *J.*  
719 *Atmos. Sci.*, **61**, 2050–2062, doi:10.1175/1520-0469(2004)061<2050:RBOTTI>2.0.CO;2.

720 Maloney, E. D., X. Jiang, S.-P. Xie, and J. J. Benedict, 2014: Process-Oriented Diagnosis of  
721 East Pacific Warm Pool Intraseasonal Variability. *J. Climate*, **27** (16), 6305–6324, doi:10.1175/  
722 JCLI-D-14-00053.1.

723 Masunaga, H., 2012: Short-term versus climatological relationship between precipitation and tro-  
724 pospheric humidity. *J. Climate*, **25**, 7983–7990, doi:10.1175/JCLI-D-12-00037.1.

725 Masunaga, H., and T. S. L’Ecuyer, 2014: A mechanism of tropical convection inferred from  
726 observed variability in the moist static energy budget. *J. Atmos. Sci.*, **71**, 3747–3766, doi:  
727 10.1175/JAS-D-14-0015.1.

728 Neelin, J. D., and I. M. Held, 1987: Modeling tropical convergence based on the moist static  
729 energy budget. *Mon. Wea. Rev.*, **115**, 3–12, doi:10.1175/1520-0493(1987)115<0003:MTCBOT>  
730 2.0.CO;2.

731 Neelin, J. D., O. Peters, and K. Hales, 2009: The transition to strong convection. *J. Atmos. Sci.*,  
732 **66**, 2367–2384, doi:10.1175/2009JAS2962.1.

733 Neelin, J. D., and J.-Y. Yu, 1994: Modes of Tropical Variability under Convective Adjustment  
734 and the Madden-Julian Oscillation. Part I: Analytical Theory. *J. Atmos. Sci.*, **51**, 1876–1894,  
735 doi:10.1175/1520-0469(1994)051<1876:MOTVUC>2.0.CO;2.

Peters, M. E., and C. S. Bretherton, 2005: A Simplified Model of the Walker Circulation with  
 an Interactive Ocean Mixed Layer and Cloud-Radiative Feedbacks. *J. Climate*, **18**, 4216–4234,  
 doi:10.1175/JCLI3534.1.

Raymond, D. J., 2000: Thermodynamic control of tropical rainfall. *Quart. J. Roy. Meteor. Soc.*,  
**126**, 889–898, doi:10.1002/qj.49712656406.

Raymond, D. J., and Ž. Fuchs, 2007: Convectively coupled gravity and moisture modes in a simple  
 atmospheric model. *Tellus A*, **59**, 627–640, doi:10.1111/j.1600-0870.2007.00268.x.

Raymond, D. J., and Ž. Fuchs, 2009: Moisture modes and the Madden-Julian oscillation. *J. Cli-*  
*mate*, **22**, 3031–3046, doi:10.1175/2008JCLI2739.1.

Raymond, D. J., S. L. Sessions, and Ž. Fuchs, 2007: A theory for the spinup of tropical depres-  
 sions. *Quart. J. Roy. Meteor. Soc.*, **133**, 1743–1754, doi:10.1002/qj.125.

Raymond, D. J., S. L. Sessions, A. H. Sobel, and Ž. Fuchs, 2009: The mechanics of gross moist  
 stability. *J. Adv. Model. Earth Syst.*, **1**, 9, doi:10.3894/JAMES.2009.1.9.

Sakaeda, N., and P. E. Roundy, 2016: Gross moist stability and the Madden-Julian Oscillation in  
 reanalysis data. *Quart. J. Roy. Meteor. Soc.*, **142**, 2740–2757, doi:10.1002/qj.2865.

Sentić, S., S. L. Sessions, and Ž. Fuchs, 2015: Diagnosing DYNAMO convection with weak  
 temperature gradient simulations. *J. Adv. Model. Earth Syst.*, **7**, 1849–1871, doi:10.1002/  
 2015MS000531.

Sessions, S. L., S. Sugaya, D. J. Raymond, and A. H. Sobel, 2010: Multiple equilibria in a cloud-  
 resolving model using the weak temperature gradient approximation. *J. Geophys. Res. Atmos.*,  
**115**, D12 110, doi:10.1029/2009JD013376.

- 757 Sobel, A., and E. Maloney, 2012: An idealized semi-empirical framework for modeling the  
758 Madden-Julian oscillation. *J. Atmos. Sci.*, **69**, 1691–1705, doi:10.1175/JAS-D-11-0118.1.
- 759 Sobel, A., and E. Maloney, 2013: Moisture modes and the eastward propagation of the MJO. *J.*  
760 *Atmos. Sci.*, **70**, 187–192, doi:10.1175/JAS-D-12-0189.1.
- 761 Sobel, A., S. Wang, and D. Kim, 2014: Moist static energy budget of the MJO during DYNAMO.  
762 *J. Atmos. Sci.*, **71**, 4276–4291, doi:10.1175/JAS-D-14-0052.1.
- 763 Sobel, A. H., and C. S. Bretherton, 2000: Modeling tropical precipitation in a single column. *J.*  
764 *Climate*, **13**, 4378–4392, doi:10.1175/1520-0442(2000)013<4378:MTPIAS>2.0.CO;2.
- 765 Sobel, A. H., and H. Gildor, 2003: A Simple Time-Dependent Model of SST Hot Spots. *J. Climate*,  
766 **16**, 3978–3992, doi:10.1175/1520-0442(2003)016<3978:ASTMOS>2.0.CO;2.
- 767 Sobel, A. H., and J. D. Neelin, 2006: The boundary layer contribution to intertropical conver-  
768 gence zones in the quasi-equilibrium tropical circulation model framework. *Theor. Comput.*  
769 *Fluid Dyn.*, **20**, 323–350, doi:10.1007/s00162-006-0033-y.
- 770 Sobel, A. H., J. Nilsson, and L. M. Polvani, 2001: The Weak Temperature Gradient Ap-  
771 proximation and Balanced Tropical Moisture Waves\*. *J. Atmos. Sci.*, **58**, 3650–3665, doi:  
772 10.1175/1520-0469(2001)058<3650:TWTGAA>2.0.CO;2.
- 773 Su, H., and J. D. Neelin, 2002: Teleconnection Mechanisms for Tropical Pacific Descent Anoma-  
774 lies during El Nino\*. *J. Atmos. Sci.*, **59**, 2694–2712, doi:10.1175/1520-0469(2002)059<2694:  
775 TMFTPD>2.0.CO;2.
- 776 Sugiyama, M., 2009: The moisture mode in the quasi-equilibrium tropical circulation model. part  
777 I: Analysis based on the weak temperature gradient approximation. *J. Atmos. Sci.*, **66**, 1507–  
778 1523, doi:10.1175/2008JAS2690.1.

Weller, R. A., and S. P. Anderson, 1996: Surface Meteorology and Air-Sea Fluxes in the Western Equatorial Pacific Warm Pool during the TOGA Coupled Ocean-Atmosphere Response Experiment. *J. Climate*, **9**, 1959–1990, doi:10.1175/1520-0442(1996)009<1959:SMAASF>2.0.CO;2.

Wentz, F., C. Gentemann, and K. Hilburn, 2015: Remote Sensing Systems TRMM TMI Daily Environmental Suite on 0.25 deg grid, Version 7.1. Remote Sensing Systems, Santa Rosa, CA, [Available online at [www.remss.com/missions/tmi](http://www.remss.com/missions/tmi)].

Wentz, F., K. Hilburn, and D. Smith, 2012: Remote Sensing Systems DMSP SSM/I Daily Environmental Suite on 0.25 deg grid, Version 7. Remote Sensing Systems, Santa Rosa, CA, [Available online at [www.remss.com/missions/ssmi](http://www.remss.com/missions/ssmi)].

Wentz, F., T. Meissner, C. Gentemann, and M. Brewer, 2014: Remote Sensing Systems AQUA AMSR-E Daily Environmental Suite on 0.25 deg grid, Version 7.0. Remote Sensing Systems, Santa Rosa, CA, [Available online at [www.remss.com/missions/amsre](http://www.remss.com/missions/amsre)].

Yanai, M., S. Esbensen, and J.-H. Chu, 1973: Determination of bulk properties of tropical cloud clusters from large-scale heat and moisture budgets. *J. Atmos. Sci.*, **30**, 611–627, doi:10.1175/1520-0469(1973)030<0611:DOBPOT>2.0.CO;2.

Yu, J., C. Chou, and J. D. Neelin, 1998: Estimating the gross moist stability of the tropical atmosphere\*. *J. Atmos. Sci.*, **55**, 1354–1372, doi:10.1175/1520-0469(1998)055<1354:ETGMSO>2.0.CO;2.

Zhang, M. H., and J. L. Lin, 1997: Constrained variational analysis of sounding data based on column-integrated budgets of mass, heat, moisture, and momentum: Approach and application to ARM measurements. *J. Atmos. Sci.*, **54**, 1503–1524, doi:10.1175/1520-0469(1997)054<1503:CVAOSD>2.0.CO;2.



801 **LIST OF TABLES**

802 **Table A1.** Characteristic GMSs. The top two rows were computed with the field campaign  
803 data, and the bottom two rows were computed with the satellite data in the same  
804 regions as TOGA COARE and DYNAMO, respectively. See the text for the  
805 definition of each quantity. . . . . 41

806 Table A1. Characteristic GMSs. The top two rows were computed with the field campaign data, and the  
807 bottom two rows were computed with the satellite data in the same regions as TOGA COARE and DYNAMO,  
808 respectively. See the text for the definition of each quantity.

Characteristic GMS	$\tilde{\Gamma}'$	$\tilde{\Gamma}$	$\gamma$
TOGA COARE (sounding)	0.257	0.263	0.217
DYNAMO (sounding)	0.171	0.195	0.187
TOGA COARE Region (satellite)	0.110	0.102	0.085
DYNAMO Region (satellite)	0.095	0.106	0.083

809

## LIST OF FIGURES

<b>Fig. 1.</b>	Flowchart of the data procedures. See the text for detail.	44
<b>Fig. 2.</b>	Spatial domains for analyses and mean precipitation from 2000 to 2007. We investigated the regions surrounded by the polygons in the four oceanic basins: the Indian Ocean (IO), the western Pacific Ocean (WP), the central-eastern Pacific Ocean (EP), and the Atlantic Ocean (AO).	45
<b>Fig. 3.</b>	(a): Binned precipitation changes as a function of the drying efficiency $\Gamma - \Gamma_C$ , averaged in 5-percentile bins of $\Gamma - \Gamma_C$ . Temporal precipitation changes $\delta \text{Pres}$ were computed with a centered difference over two days. (b): Probabilities of increase in precipitation as a function of $\Gamma - \Gamma_C$ , computed in the same bins as (a). (c): Binned precipitation as a function of $\Gamma - \Gamma_C$ , computed in the same way as above. Each analysis was conducted within the domains depicted in Fig. 2, IO (red), WP (green), EP (black), and AO (blue).	46
<b>Fig. 4.</b>	(Left column): Scatter plots of diabatic source ( $D \equiv \langle Q_R \rangle + S$ ) against divergence of column DSE ( $+\nabla \cdot \langle s\mathbf{v} \rangle$ ) over the four oceanic basin regions: (a) IO, (c) WP, (e) EP, and (g) AO. (Right column): As in the left panels, but for divergence of column MSE ( $+\nabla \cdot \langle h\mathbf{v} \rangle$ ). In each panel, the black dashed line was computed with the regression through the origin, and the gray line was computed with the binning average. The blue cross mark indicates the mean value.	47
<b>Fig. 5.</b>	As in Fig. 3, but the critical GMS $\Gamma_C$ was replaced with the slopes of the regression lines $\gamma$ in the left panels of Fig. 4.	48
<b>Fig. 6.</b>	(a)–(d): Probabilities of increase in precipitation within grids of $\nabla \cdot \langle h\mathbf{v} \rangle$ and $\nabla \cdot \langle s\mathbf{v} \rangle$ over the four oceanic basins. The probabilities were calculated within $50 \text{ Wm}^{-2} \times 50 \text{ Wm}^{-2}$ grids. The black dashed lines and the gray lines are identical to those in the left panels of Fig. 4.	49
<b>Fig. 7.</b>	(a)–(d): Mean values of temporal changes of $\nabla \cdot \langle h\mathbf{v} \rangle$ and $\nabla \cdot \langle s\mathbf{v} \rangle$ (with a centered difference) at each grid in the GMS plane, represented in vector arrows, over the four domains. The mean values were calculated within $100 \text{ Wm}^{-2} \times 100 \text{ Wm}^{-2}$ grids. The dashed lines are identical to those in the left panels of Fig. 4 and Fig. 6.	50
<b>Fig. 8.</b>	(a): As in Fig. 6, but for the whole tropical convergence zone with the mean precipitation greater than 5 mm/day (the colored regions in Fig. 9). (b): As in Fig. 7, but for the whole tropical convergence zone. The slope of the black dashed line was computed similarly to that in Figs. 6 and 7, and the two gray lines represent the geographic variability of the critical GMS.	51
<b>Fig. 9.</b>	(a): Critical GMS ( $\gamma$ in Eq. 15) map over the oceanic regions with the mean precipitation greater than 5 mm/day. (b): Map of anomalous characteristic GMS ( $\tilde{\Gamma}'$ in Eq. 17). (c): Map of non-anomalous characteristic GMS ( $\tilde{\Gamma}$ in Eq. 18). (d): Map of climatological GMS ( $\bar{\Gamma}$ in Eq. 19). It should be cautioned that the color scales are different among the different panels.	52
<b>Fig. 10.</b>	(a): Time-series of precipitation rate during DYNAMO. (b): Phase transitions of three MJO events shown in different colors during DYNAMO in the GMS plane. All variables are 10-day running averages. The DYNAMO field campaign was conducted from October 2011 to the end of December. Plotted are data averaged over the northern sounding array.	53
<b>Fig. 11.</b>	(a): one cycle [the start (red dot) to the end (blue dot)] of $\langle \omega \partial h / \partial p \rangle'$ and $P'$ expressed as Eqs. 23 and 24. For an illustrative purpose, we plotted from day 20 to day 60. $\Gamma_{v,r}$ and $\Gamma_{v,i}$	

852 were set to be 0.25 and 0.15, respectively, with  $\Gamma_{\text{eff},r} = 0$ . (b): Three cycles (from day 20  
853 to day 140) with  $\Gamma_{\text{eff},r} = -0.01$ . . . . . 54

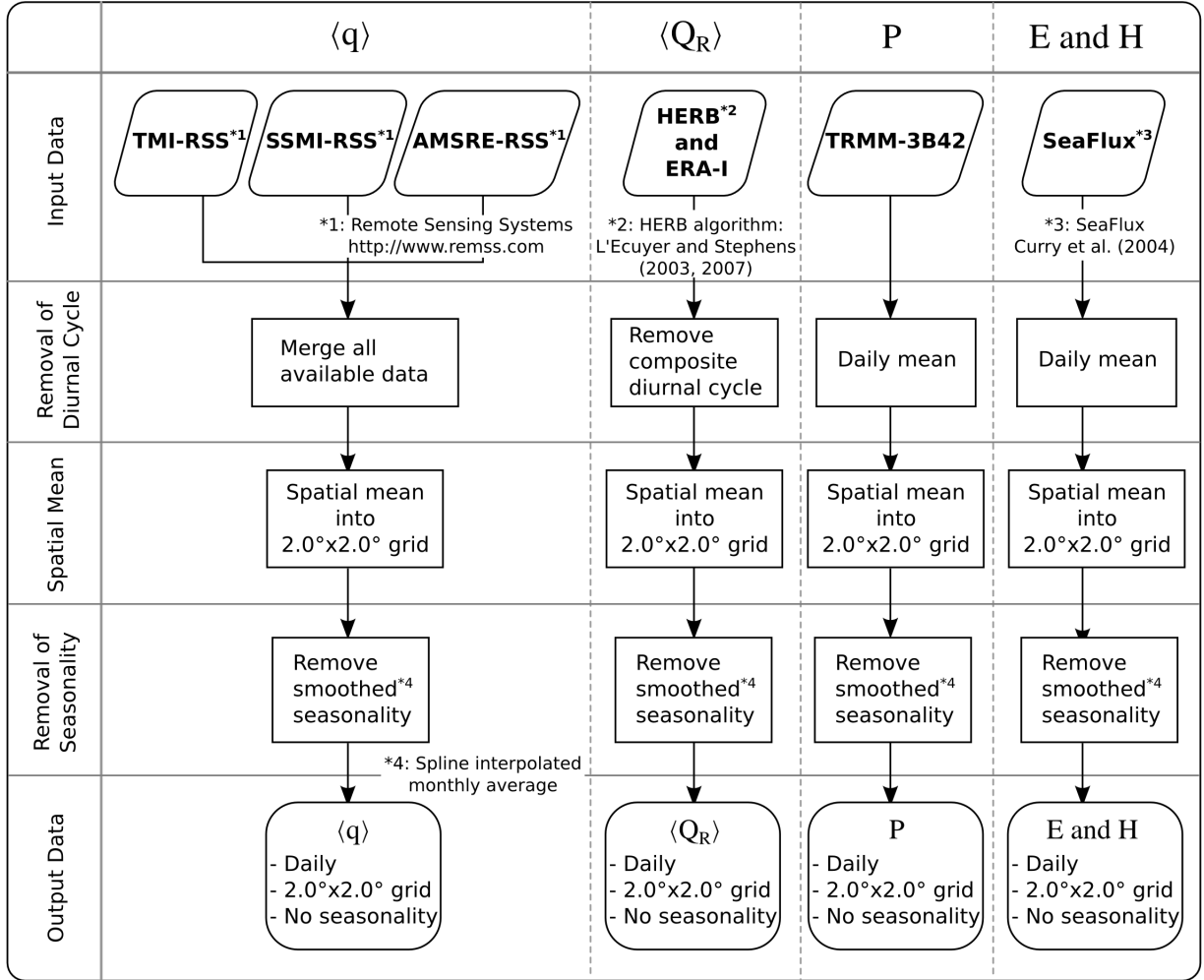


FIG. 1. Flowchart of the data procedures. See the text for detail.

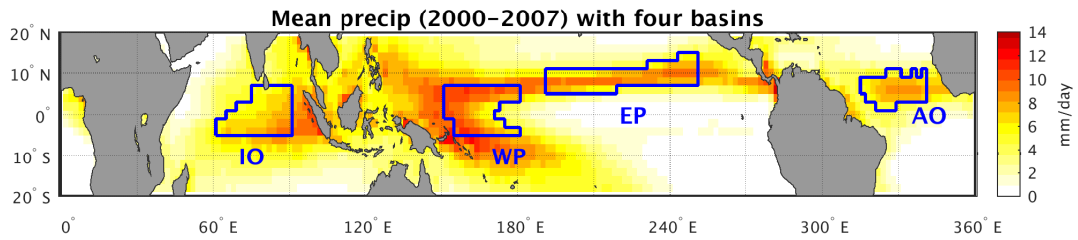


FIG. 2. Spatial domains for analyses and mean precipitation from 2000 to 2007. We investigated the regions surrounded by the polygons in the four oceanic basins: the Indian Ocean (IO), the western Pacific Ocean (WP), the central-eastern Pacific Ocean (EP), and the Atlantic Ocean (AO).

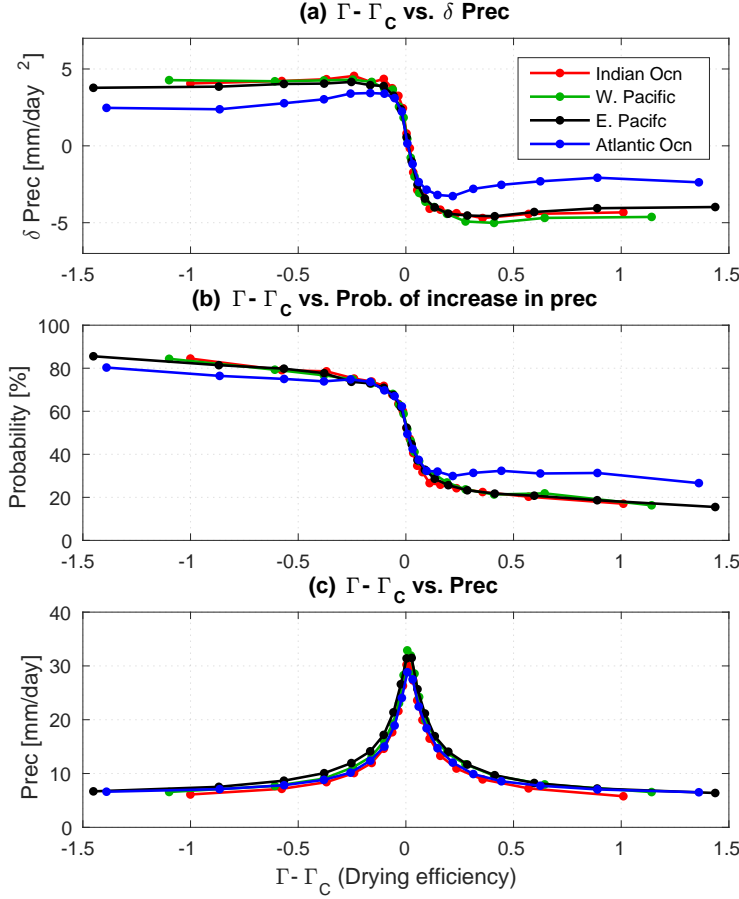


FIG. 3. (a): Binned precipitation changes as a function of the drying efficiency  $\Gamma - \Gamma_C$ , averaged in 5-percentile bins of  $\Gamma - \Gamma_C$ . Temporal precipitation changes  $\delta$  Prec were computed with a centered difference over two days. (b): Probabilities of increase in precipitation as a function of  $\Gamma - \Gamma_C$ , computed in the same bins as (a). (c): Binned precipitation as a function of  $\Gamma - \Gamma_C$ , computed in the same way as above. Each analysis was conducted within the domains depicted in Fig. 2, IO (red), WP (green), EP (black), and AO (blue).

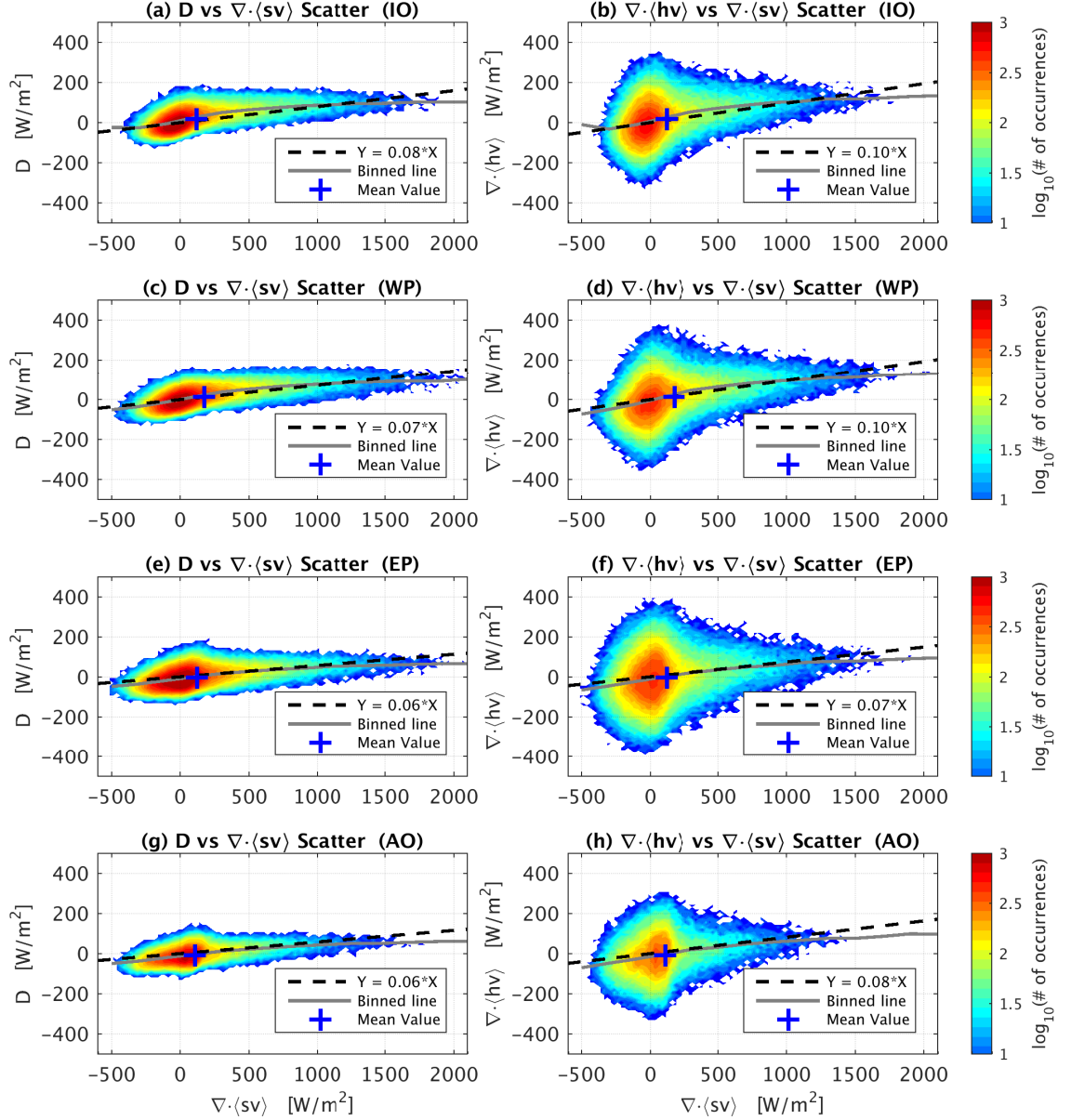


FIG. 4. (Left column): Scatter plots of diabatic source ( $D \equiv \langle Q_R \rangle + S$ ) against divergence of column DSE ( $+\nabla \cdot \langle \mathbf{sv} \rangle$ ) over the four oceanic basin regions: (a) IO, (c) WP, (e) EP, and (g) AO. (Right column): As in the left panels, but for divergence of column MSE ( $+\nabla \cdot \langle \mathbf{hv} \rangle$ ). In each panel, the black dashed line was computed with the regression through the origin, and the gray line was computed with the binning average. The blue cross mark indicates the mean value.



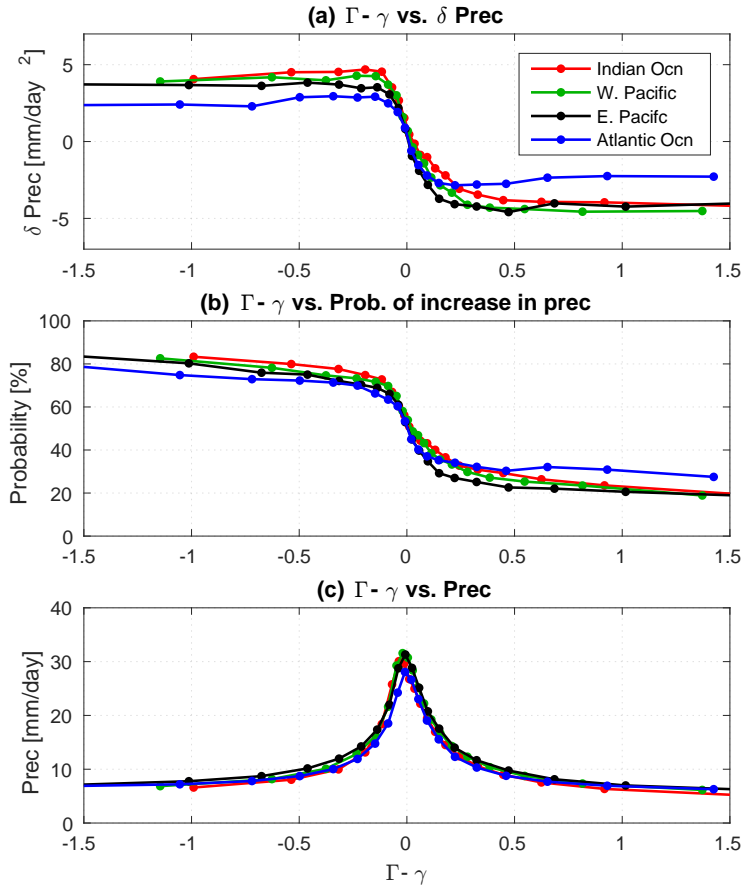


FIG. 5. As in Fig. 3, but the critical GMS  $\Gamma_C$  was replaced with the slopes of the regression lines  $\gamma$  in the left panels of Fig. 4.

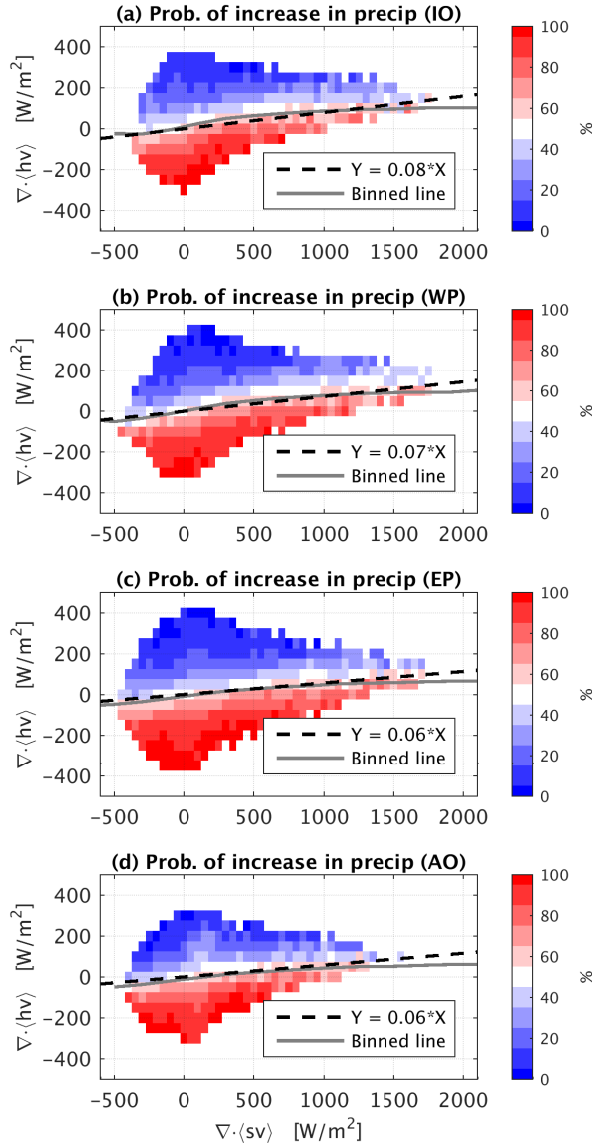


FIG. 6. (a)–(d): Probabilities of increase in precipitation within grids of  $\nabla \cdot \langle hv \rangle$  and  $\nabla \cdot \langle sv \rangle$  over the four oceanic basins. The probabilities were calculated within  $50 \text{ Wm}^{-2} \times 50 \text{ Wm}^{-2}$  grids. The black dashed lines and the gray lines are identical to those in the left panels of Fig. 4.

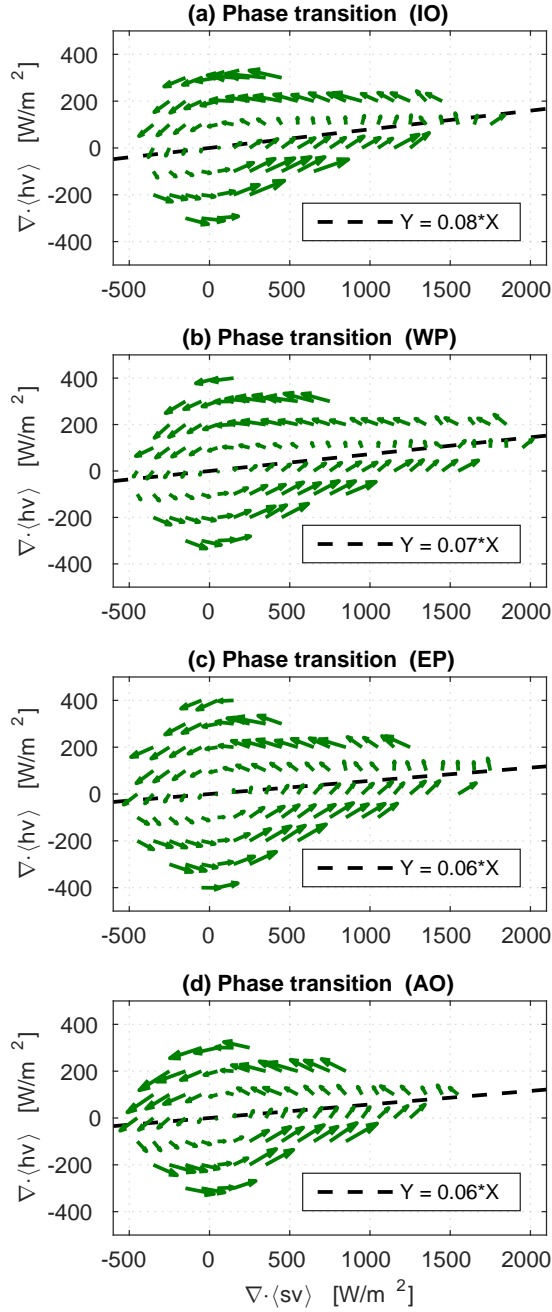


FIG. 7. (a)–(d): Mean values of temporal changes of  $\nabla \cdot \langle hv \rangle$  and  $\nabla \cdot \langle sv \rangle$  (with a centered difference) at each grid in the GMS plane, represented in vector arrows, over the four domains. The mean values were calculated within  $100 \text{ Wm}^{-2} \times 100 \text{ Wm}^{-2}$  grids. The dashed lines are identical to those in the left panels of Fig. 4 and Fig. 6.

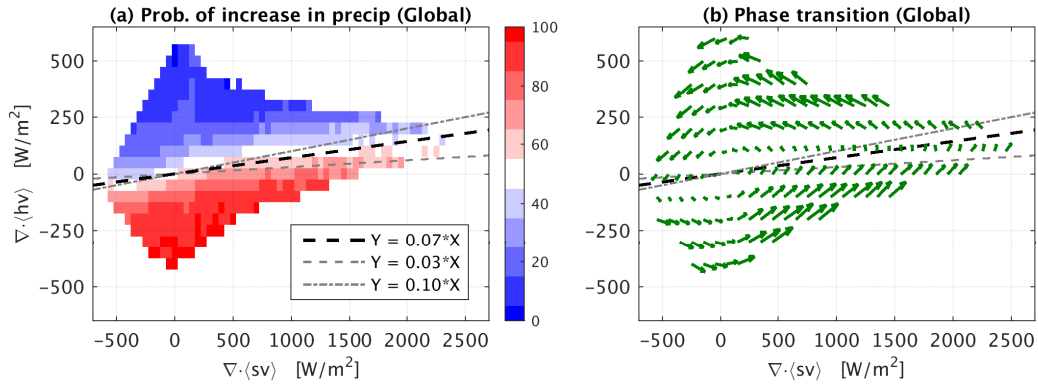


FIG. 8. (a): As in Fig. 6, but for the whole tropical convergence zone with the mean precipitation greater than 5 mm/day (the colored regions in Fig. 9). (b): As in Fig. 7, but for the whole tropical convergence zone. The slope of the black dashed line was computed similarly to that in Figs. 6 and 7, and the two gray lines represent the geographic variability of the critical GMS.

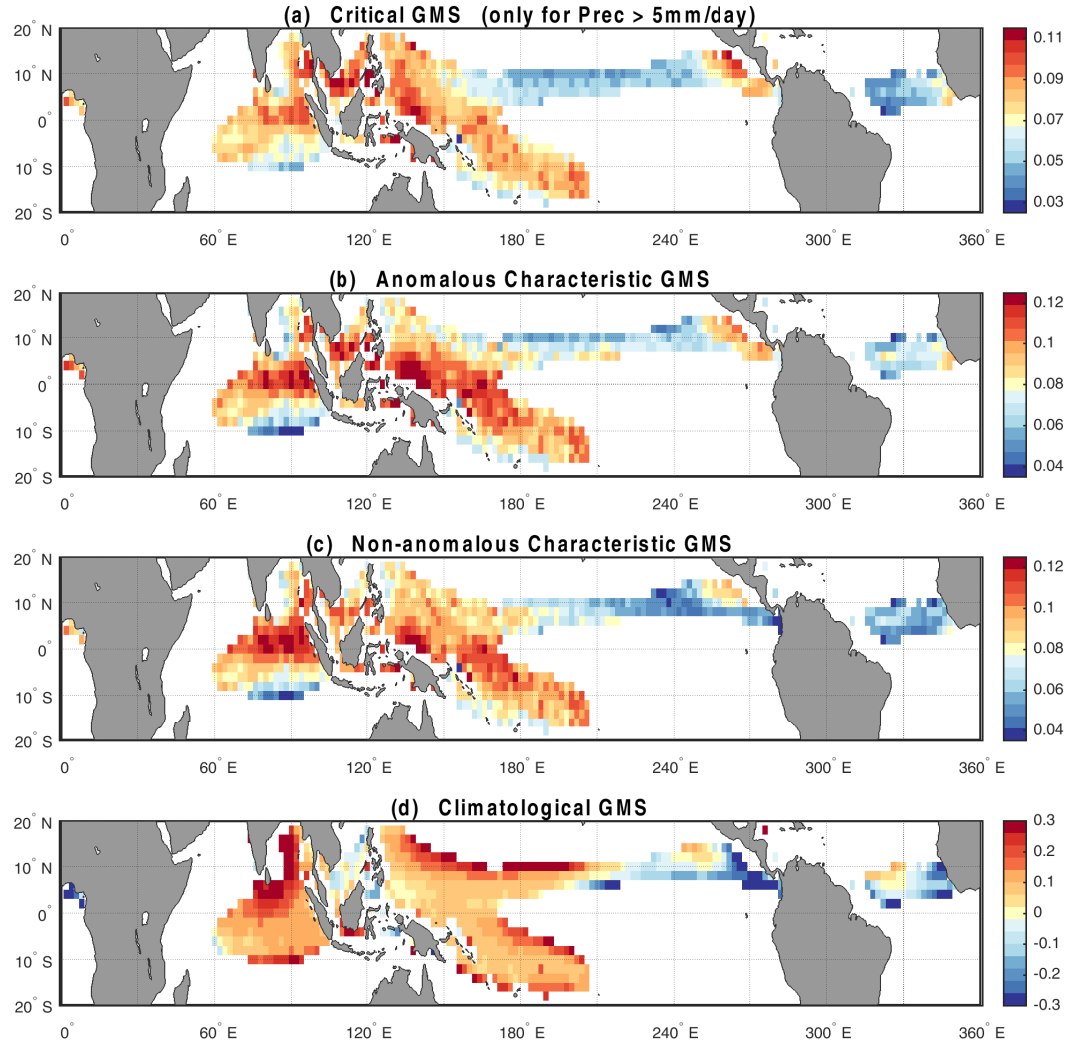


FIG. 9. (a): Critical GMS ( $\gamma$  in Eq. 15) map over the oceanic regions with the mean precipitation greater than 5 mm/day. (b): Map of anomalous characteristic GMS ( $\tilde{\Gamma}'$  in Eq. 17). (c): Map of non-anomalous characteristic GMS ( $\tilde{\Gamma}$  in Eq. 18). (d): Map of climatological GMS ( $\bar{\Gamma}$  in Eq. 19). It should be cautioned that the color scales are different among the different panels.

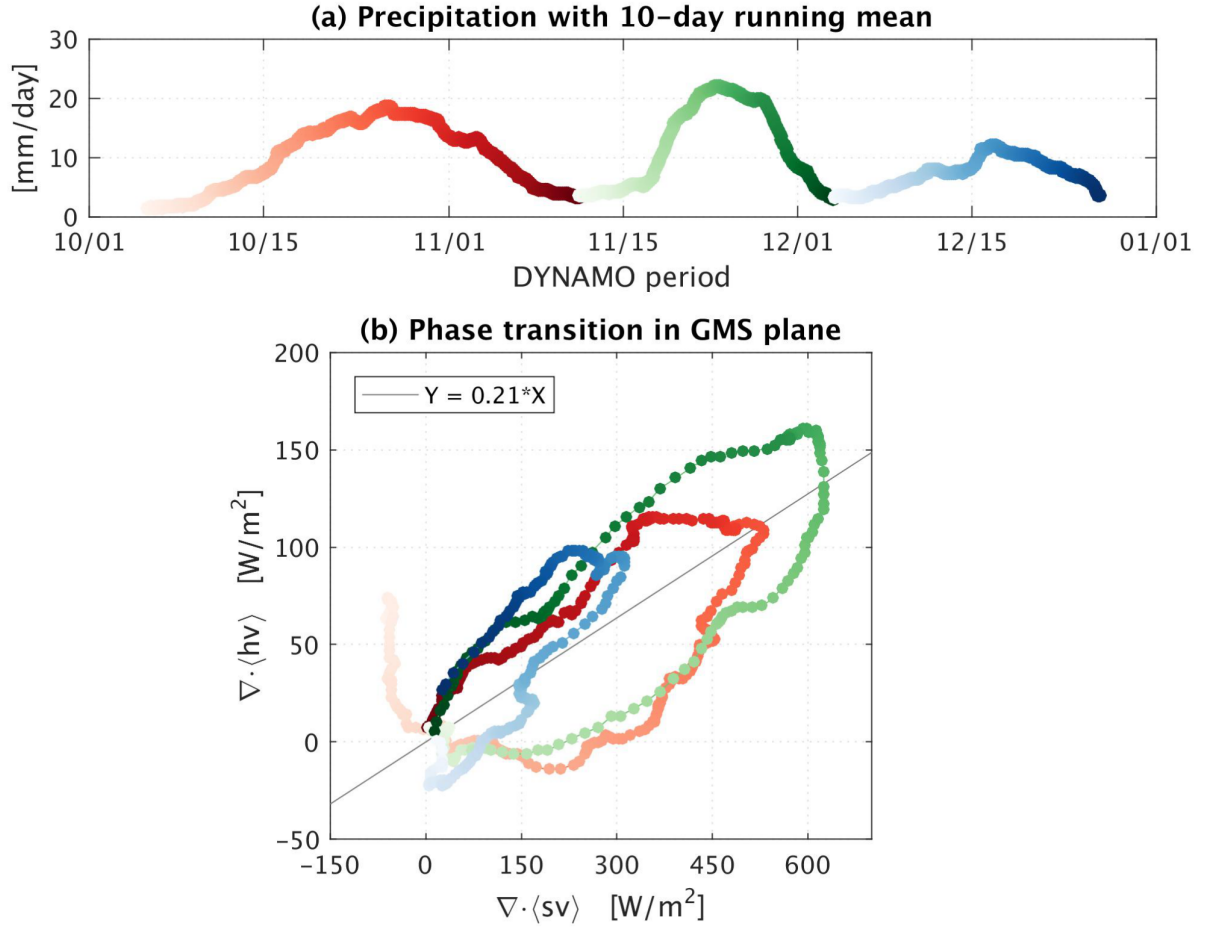


FIG. 10. (a): Time-series of precipitation rate during DYNAMO. (b): Phase transitions of three MJO events shown in different colors during DYNAMO in the GMS plane. All variables are 10-day running averages. The DYNAMO field campaign was conducted from October 2011 to the end of December. Plotted are data averaged over the northern sounding array.

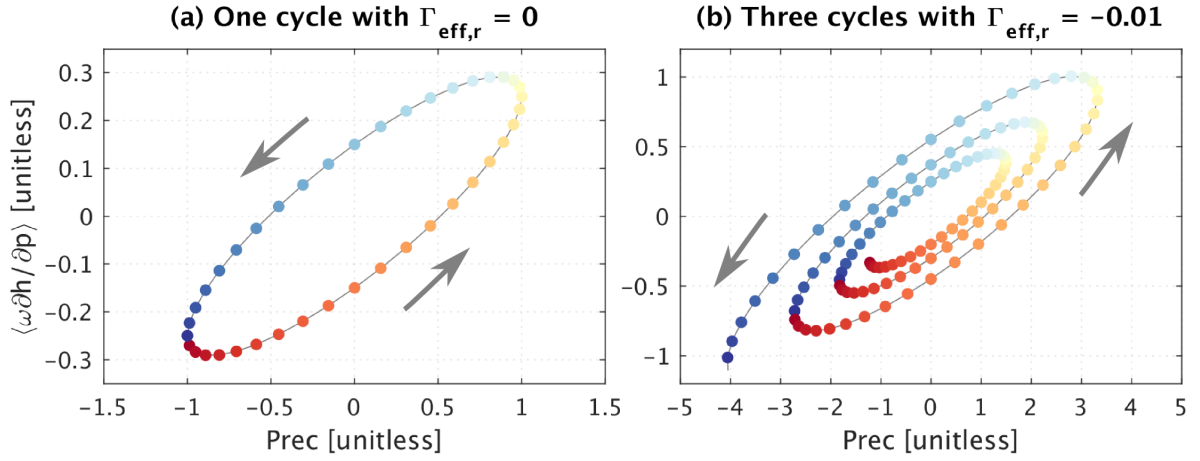


FIG. 11. (a): one cycle [the start (red dot) to the end (blue dot)] of  $\langle \omega \partial h / \partial p \rangle'$  and  $P'$  expressed as Eqs. 23 and 24. For an illustrative purpose, we plotted from day 20 to day 60.  $\Gamma_{v,r}$  and  $\Gamma_{v,i}$  were set to be 0.25 and 0.15, respectively, with  $\Gamma_{\text{eff},r} = 0$ . (b): Three cycles (from day 20 to day 140) with  $\Gamma_{\text{eff},r} = -0.01$ .